

Electronic layer decoupling driven by density-wave order in $\text{La}_4\text{Ni}_3\text{O}_{10}$

Ziqiang Guan,^{1,*} Sophia F. R. TenHuisen,^{1,2,*} M. Tepie,¹ Yifeng Zhao,³ Ezra Day-Roberts,³ Harrison LaBollita,³ Alexander M. Young,¹ Xiaomeng Cui,¹ Xinglong Chen,⁴ Filippo Glerean,^{1,5} Carl Audric Guia,¹ Mark P. M. Dean,⁵ Philip Kim,^{1,2} J. F. Mitchell,⁴ Antia S. Botana,³ Christopher C. Homes,⁶ and Matteo Mitrano^{1,†}

¹*Department of Physics, Harvard University, Cambridge, Massachusetts 02138, USA*

²*John A. Paulson School of Engineering and Applied Sciences, Harvard University, Cambridge, Massachusetts 02138, USA*

³*Department of Physics, Arizona State University, Tempe, Arizona 85287, USA*

⁴*Materials Science Division, Argonne National Laboratory, Lemont, Illinois 60439, USA*

⁵*Condensed Matter Physics and Materials Science Department, Brookhaven National Laboratory, Upton, New York 11973, USA*

⁶*National Synchrotron Light Source II, Brookhaven National Laboratory, Upton, NY, USA*

(Dated: January 15, 2026)

We probe the density-wave transition of the trilayer nickelate $\text{La}_4\text{Ni}_3\text{O}_{10}$ with polarization-resolved infrared spectroscopy. The low-energy electrodynamics is strongly anisotropic, with metallic in-plane and insulating out-of-plane character. In the ordered phase, the anisotropy grows more than an order of magnitude as the out-of-plane conductivity is sharply suppressed. We interpret this enhancement as an effective electronic decoupling of the Ni-O layers, driven by a spin-density-wave-induced redistribution of $\text{Ni-}d_{z^2}$ occupation within the trilayers. This electronic response is accompanied by clear shifts and splittings of the out-of-plane phonons, compatible with a density-wave instability of electronic origin.

Bilayer $\text{La}_3\text{Ni}_2\text{O}_7$ and trilayer $\text{La}_4\text{Ni}_3\text{O}_{10}$ Ruddlesden-Popper (RP) nickelates become superconductors under pressure [1–9]. In both of these materials, superconductivity emerges from density-wave (DW) ground states at ambient pressure, seemingly emulating the phenomenology of hole-doped copper oxides [10–15]. However, unlike high- T_c cuprates, whose low-energy physics is often captured by a single $d_{x^2-y^2}$ band, RP nickelates are multiorbital systems with substantial interlayer coupling. It is therefore crucial to resolve how the active orbitals contribute to the DW instabilities, mediate coupling between Ni-O planes, and influence the transport properties of these materials [9, 16, 17].

The trilayer RP compound $\text{La}_4\text{Ni}_3\text{O}_{10}$, shown in Fig. 1(a), is a compelling platform to address these multiorbital effects. This material has an average Ni valence of $3d^{7.33}$, and both $d_{x^2-y^2}$ and d_{z^2} orbitals contribute to its low-energy physics [18–23]. While $d_{x^2-y^2}$ orbitals are key to the in-plane physics, d_{z^2} states couple the three NiO_3 octahedral layers via apical-oxygen hybridization. This out-of-plane coupling also differentiates inner (light purple) and outer (dark purple) Ni-O layers due to their distinct local electronic environments [21, 23–25]. At ambient pressure, $\text{La}_4\text{Ni}_3\text{O}_{10}$ exhibits an intertwined spin- and charge-density-wave (SDW, CDW) transition near $T_{\text{DW}} \approx 140$ K. The CDW is in phase across all three layers, while the SDW resides on the two antiferromagnetically-coupled outer layers, leaving a node in the inner layer [13, 17, 21]. Under pressure, CDW and SDW states collapse, with superconductivity appearing at $T_c \approx 20 - 40$ K [3, 6, 14].

In this Letter, we use infrared spectroscopy to investigate how the DW phase influences the low-energy elec-

trodynamics in trilayer nickelate $\text{La}_4\text{Ni}_3\text{O}_{10}$ bulk single crystals. Details on single-crystal sample growth, optical measurements, and computational simulations can be found in the Supplementary Material [26]. We observe a pronounced electronic anisotropy at far-infrared frequencies, as the in-plane conductivity is metallic, while the conductivity in the out-of-plane stacking c^* direction is insulating. Across the DW transition, the out-of-plane transport is strongly suppressed, yielding an order-of-magnitude enhancement of the transport anisotropy. We attribute this effect to a DW-driven redistribution of Ni d_{z^2} orbital occupation that effectively decouples the Ni-O layers. We also observe distinct phonon renormalizations and mode splitting, consistent with the presence of electron-phonon and magneto-elastic coupling. Together, these results show that the DW phase dramatically reshapes the normal-state properties of RP nickelates.

Figure 1(b) shows the polarized infrared reflectivity of $\text{La}_4\text{Ni}_3\text{O}_{10}$ for in-plane ($E \parallel ab$) and out-of-plane ($E \parallel c^*$) directions over a broad frequency range. Here, c^* denotes the direction normal to the ab -plane, which is slightly tilted relative to the crystallographic c axis in the monoclinic $P2_1/a$ structure. The optical response of this trilayer nickelate is strongly anisotropic. The in-plane reflectivity is metallic, exceeding 0.9 below 500 cm^{-1} and exhibiting a clear plasma edge around 10,000 cm^{-1} . In contrast, the out-of-plane reflectivity is nearly insulating, with only a minor conductivity contribution (likely from hopping conduction) and several infrared-active phonons. This qualitative dichotomy mirrors layered cuprates, where metallic CuO_2 planes coexist with a nearly insulating interlayer response [27]. Fig. 1(c) shows the optical conductivity from Kramers-Kronig transfor-

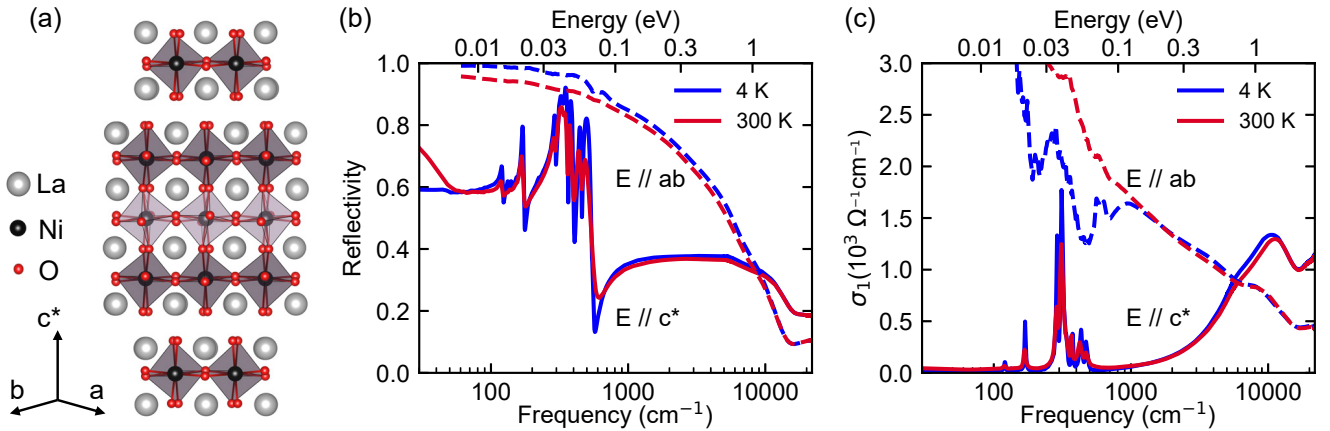


FIG. 1. (a) Structure of the trilayer Ruddlesden-Popper nickelate La₄Ni₃O₁₀, consisting of three NiO₃ octahedral layers, where the inner and outer layers are colored differently to reflect their distinct local electronic environment. (b) Reflectivity and (c) real part of the optical conductivity σ_1 at base (blue) and room temperature (red). Out-of-plane ($E \parallel c^*$) and in-plane ($E \parallel ab$) optical responses are shown in solid lines and broken lines, respectively. The DW transition temperature is approximately 140 K.

mations [28, 29] (see Supplementary Material Sec. S1). The optical absorption reveals that the large electronic anisotropy surprisingly reverses around 5000 cm⁻¹. At low frequencies the in-plane conductivity dominates, consistent with quasi-two-dimensional metallicity, whereas at higher energies the out-of-plane conductivity exceeds the in-plane component. This crossover signals a clear energy-scale separation of orbital excitations. The high-energy response is set by strong out-of-plane coupling mediated by Ni d_{z^2} orbitals, while the low-energy electrodynamics is dominated by in-plane Ni $d_{x^2-y^2}$, with a substantially reduced d_{z^2} contribution [21].

The observed frequency-dependent reversal in the optical anisotropy is unusual among layered correlated materials. In cuprate superconductors, the infrared optical response is dominated by in-plane $d_{x^2-y^2}$ orbitals, while the out-of-plane conductivity is suppressed by roughly an order of magnitude across the entire infrared range without signs of anisotropy reversals [27, 30–33]. In iron-based superconductors, despite their multiorbital and more three-dimensional electronic structure, the in-plane conductivity still exceeds the out-of-plane response, with anisotropy ratios typically ranging between 1 and 10 and, again, no reported reversal [34–37]. The anisotropy reversal of our trilayer nickelate thus reflects a marked multiorbital nature, where distinct orbitals dominate the electronic properties at different energy scales, akin to earlier reports on La_{2-x}Sr_xNiO₄ and theoretical predictions for La₃Ni₂O₇ [38, 39].

Below the DW transition, the in-plane optical conductivity remains metallic, but shows a partial mid-infrared depletion of spectral weight associated with opening of a DW gap [Fig. 1(c)]. We extract the DW gap by analyzing the differential optical conductivity (see Supplementary

Sec. S3). At base temperature, we obtain an energy gap $2\Delta_{\text{DW}} = 112$ meV, corresponding to $2\Delta_{\text{DW}}/k_B T_{\text{DW}} \approx 9.3$. This ratio is well above the weak-coupling value of 3.52, yet comparable to that of La₃Ni₂O₇ [40], and consistent with earlier estimates for La₄Ni₃O₁₀ [16, 41–43]. A full temperature dependence, shown in Supplementary Fig. S1, verifies that this change occurs continuously. The gap $\Delta(T)$ follows a mean-field behavior, in line with prior X-ray diffraction and neutron scattering [13], and points to a second-order transition, likely driven by an SDW instability [44].

Figures 2(a)-(d) show the main result of our work, where we observe a dramatic effect of the density wave on the temperature dependence of the low-frequency in- and out-of-plane optical conductivity. At frequencies below the phonon and interband contributions, we simultaneously fit the real and imaginary optical conductivity with a simplified Drude+ ε_∞ model, and obtain extrapolated DC resistivities ρ_{ab} and ρ_{c^*} from $\rho_{\text{dc}} = \lim_{\omega \rightarrow 0} 1/\sigma_1(\omega)$ at each temperature [Fig. 2(e)]. While ρ_{ab} remains metallic across the entire temperature range, showing only a weak kink at T_{DW} , ρ_{c^*} rises abruptly by nearly a factor of five upon cooling through T_{DW} . As a result, the anisotropy ratio ρ_{c^*}/ρ_{ab} [Fig. 2(f), inset] grows by over an order of magnitude, from $\rho_{c^*}/\rho_{ab} \simeq 70$ at room temperature to $\rho_{c^*}/\rho_{ab} \simeq 2600$ at 4 K, with the sharpest enhancement occurring at the DW transition. We also note that these optically extrapolated DC resistivities agree with separately measured DC transport measurement results (shown as broken lines in Fig. 2(e)). These results show that the DW transition drives a strongly anisotropic reorganization of charge dynamics, with out-of-plane transport suppressed far more than that in-plane. The large and strongly temperature-dependent

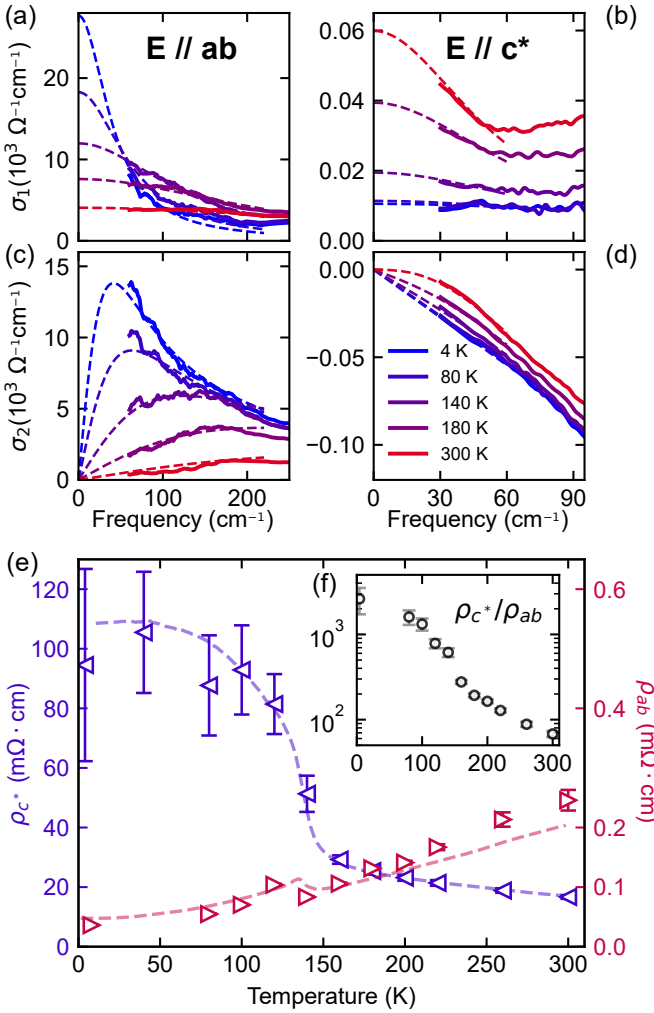


FIG. 2. (a)-(d) Temperature-dependent real and imaginary optical conductivity of $\text{La}_4\text{Ni}_3\text{O}_{10}$ in- ($E \parallel ab$) and out-of-plane ($E \parallel c^*$), denoted as solid lines. Drude+ ε_∞ model fits are shown as dashed lines. (e) Temperature dependence of the extrapolated DC resistivity obtained from the Drude fits. Left- and right-pointing triangles with error bars represent the out-of-plane (ρ_c^*) and in-plane (ρ_{ab}) resistivities, respectively. Broken lines denote DC resistivity obtained from transport measurements. ρ_{ab} is adapted from Ref. [45] (see Supplementary Material Sec. S6 for further details). (f) Inset: Temperature-dependent resistivity anisotropy ratio ρ_c^*/ρ_{ab} .

anisotropy is consistent with an effective dimensional crossover, meaning that the electronic properties transition from a moderately three-dimensional character at high-temperature to a highly two-dimensional character in the low-temperature DW phase.

We argue that the enhanced electronic anisotropy follows from an effective decoupling of the layers within each trilayer subunit (Fig. 3). In trilayer RP nickelates, strong interlayer hybridization of the Ni d_{z^2} orbitals produces three molecular subbands (bonding, nonbonding, antibonding) quantum-confined by La–O spacer layers

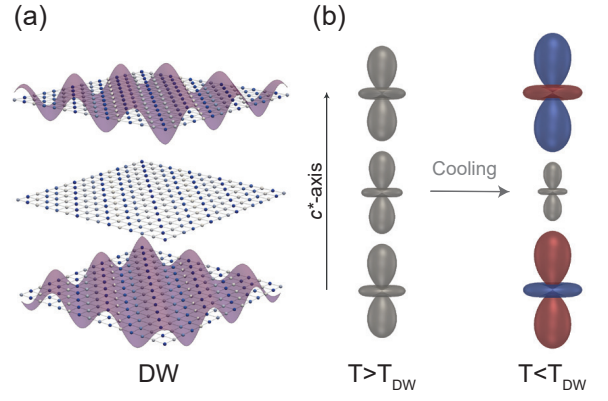


FIG. 3. (a) Real-space depiction of the DW modulation. Below T_{DW} , an antiphase SDW develops on the outer layers, leaving the inner layer as a magnetic node, while the intertwined CDW is in-phase across the trilayer. The SDW is indicated by the purple wave, and the CDW by the blue/white variation of the lattice color. (b) Proposed qualitative schematic of DW-driven redistribution of Ni d_{z^2} orbital occupation within a trilayer. Above T_{DW} the trilayer is nonmagnetic and the d_{z^2} occupation is comparable in inner and outer Ni–O layers despite their inequivalent local environments. Below T_{DW} , the SDW residing on the outer layers (with a magnetic node on the inner layer) is accompanied by an enhanced d_{z^2} weight on the outer layers and a reduced weight on the inner layer, thereby suppressing interlayer transport. The inverted colors on the outer layer d_{z^2} orbitals illustrate the phase of the SDW modulation.

between successive Ni–O trilayers. The bonding and antibonding states carry d_{z^2} weight on all three layers, whereas the odd-symmetry nonbonding band has a node on the inner Ni layer. As a result, layer-differentiated filling of the d_{z^2} orbitals emerges naturally in this system, independent of temperature [21, 22, 25, 46, 47]. Upon cooling into the DW state, $\text{La}_4\text{Ni}_3\text{O}_{10}$ develops an intertwined SDW–CDW state in which the SDW resides on the two outer Ni–O layers, leaving a node on the nonmagnetic inner layer [13] [Fig. 3(a)]. Concomitantly, the DW redistributes orbital weight across the trilayer and promotes the nonbonding component, thus increasing d_{z^2} occupation on the outer layers while lowering it on the inner layer [21, 48] [Fig. 3(b)]. This redistribution reduces the effective interlayer overlap of the d_{z^2} orbitals, and suppresses out-of-plane charge transport.

This electronic layer decoupling is supported by the kinetic-energy renormalization $K_{\text{exp}}/K_{\text{DFT}}$ (Supplementary Sec. §4), where K_{exp} is obtained from the Drude plasma frequency and K_{DFT} from uncorrelated DFT. At 160 K (above T_{DW}) we find $K_{\text{exp}}^{ab}/K_{\text{DFT}}^{ab} = 0.237$, consistent with a moderately correlated metal [41, 49], while the c^* -axis renormalization is far stronger, $K_{\text{exp}}^{c^*}/K_{\text{DFT}}^{c^*} = 0.032$. The resulting anisotropy implies that c^* -axis charge dynamics, set by d_{z^2} -mediated interlayer hopping, is already strongly correlated at high temperature and

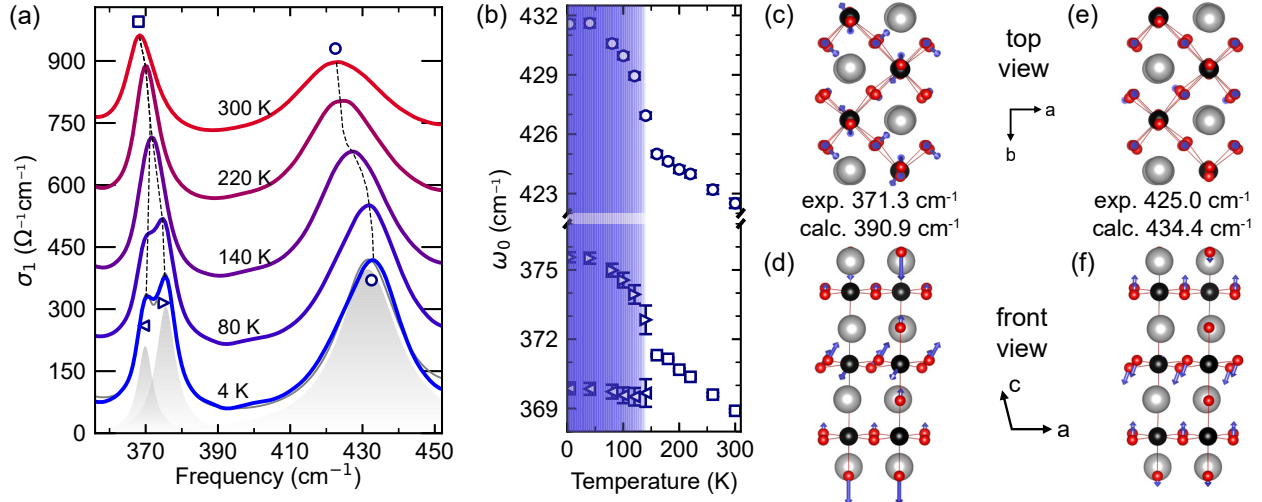


FIG. 4. (a) Temperature evolution of the out-of-plane vibrational response. Spectra are vertically offset by $150 \Omega^{-1}\text{cm}^{-1}$ for clarity. Symbols mark phonon frequencies and dotted lines are guides to the eye. Drude-Lorentz fits to the 4 K spectrum with individual contributions are shown as grey lines and shaded areas, respectively. (b) Temperature-dependent phonon frequencies for selected modes; triangles denote split modes in the DW phase (blue shading). (c)-(f) Calculated atomic displacements for infrared-active modes matching the 160 K data in panel (b); only large-amplitude displacements are shown for clarity. Owing to the monoclinic angle β , the crystallographic c axis is tilted by $\sim 11^\circ$ relative to the experimental out-of-plane c^* direction. (c)-(d) and (e)-(f) are views of the same mode from two different directions.

thus especially susceptible to the DW transition, consistent with the observed layer decoupling. Changes in quasiparticle coherence [50] and/or a possible partial gap opening on d_{z^2} -derived states [51] may further suppress the low-energy c^* -axis response in the DW state.

The pronounced enhancement of the low energy electronic anisotropy highlights the distinctive place of RP nickelates within the landscape of unconventional superconductors. Cuprates typically display very large, strongly temperature-dependent electronic anisotropy, sometimes accompanied by signatures of a dimensional crossover toward a highly two-dimensional low-energy state [52–59]. However, their physics is effectively described by a single $d_{x^2-y^2}$ orbital. By contrast, iron-based superconductors, where multiple orbitals contribute comparably to both in-plane and out-of-plane transport, exhibit only moderate anisotropy with weak temperature dependence [36, 60–67]. Our data show that La₄Ni₃O₁₀ realizes an intermediate regime where several orbitals remain active near E_F and interlayer coupling is appreciable. Yet once DW order sets in, it sharply amplifies the transport anisotropy by effectively decoupling the Ni-O layers within each trilayer subunit, enhancing the two-dimensional character of the low-energy charge dynamics [8, 68].

Beyond reshaping the low-energy electrodynamics, the DW transition also imprints clear signatures in the c^* -axis vibrational spectrum. Analysis of the infrared-active phonons (see Supplementary Sec. S9) shows that

the strongest effects occur between 350 and 450 cm⁻¹ [Figs. 4(a)-(b)]. Upon cooling into the DW state, the 370 cm⁻¹ mode splits into two branches, while the 430 cm⁻¹ mode strongly hardens without splitting [Fig. 4(b)]. Additionally, weaker anomalies are discussed in the Supplementary Material Sec. S9, but in all cases the low-temperature evolution departs significantly from the smooth anharmonic trends above T_{DW} . We compared the room-temperature results to first-principles calculations for the monoclinic $P2_1/a$ crystal symmetry. Based on this analysis, we associate the phonons at 371 and 425 cm⁻¹ to the calculated eigenvectors in Figs. 4(c)-(f). These are dominated by Ni-O bond distortions with mixed bending and stretching, implying that the DW primarily perturbs lattice distortions coupled to charge modulation in the Ni-O layers.

These vibrational anomalies could originate from (i) a structural transition, (ii) zone folding by the DW superlattice, (iii) electron-phonon coupling, or (iv) magnetoelastic coupling. Across the DW transition, the crystal structural symmetry remains unchanged and the reported lattice-parameter anomalies are well below the 0.1% level [45, 69–71], yet we observe $\sim 1\%$ frequency shifts and splittings only for certain phonons in a frequency window of 300–500 cm⁻¹, far exceeding expectations from such small structural changes. This mismatch, together with the absence of structural symmetry lowering, disfavors an explanation based on a simple lattice instability. Zone folding by the DW superlattice,

which back-folds finite-momentum phonons to the zone center [72], is likewise inconsistent with our data. The DW in $\text{La}_4\text{Ni}_3\text{O}_{10}$ is incommensurate, so any folded spectral weight would be broadly distributed and likely too weak to yield sharp new modes. Even approximating the DW by its closest five-unit-cell periodicity would generically activate many additional modes across the spectrum. Instead, we observe clear DW anomalies and only in a small subset of Ni–O vibrations. Electron-phonon coupling in the DW state is a more compelling mechanism. The CDW is out of phase between neighboring trilayers [13], effectively doubling the electronic periodicity along c^* and introducing a mode degeneracy that can be lifted by DW-driven electronic renormalization. The unidirectional CDW in the Ni–O layers creates an anisotropic charge distribution [13], which can alter the elastic constants along orthogonal Ni–O directions and split selected Ni–O modes. Magnetoelastic coupling may also contribute by renormalizing phonon energies and lifetimes and, in some cases, producing mode splitting [73]. Because the CDW in $\text{La}_4\text{Ni}_3\text{O}_{10}$ is intertwined with SDW order [42, 44], and the phonon anomalies occur at energies comparable to magnetic excitations (up to ~ 50 meV) [74], coupling between lattice vibrations and collective spin excitations is a realistic possibility.

In the aggregate, our observations establish $\text{La}_4\text{Ni}_3\text{O}_{10}$ as a strongly anisotropic, multiorbital metal. Upon entering the DW state, its low-energy anisotropy increases by over an order of magnitude, consistent with an effective decoupling of the Ni–O layers within each trilayer subunit. The simplest reading of the optical data is that this process is electronically driven, arising from a DW-induced redistribution of Ni d_{z^2} occupation that quenches interlayer charge dynamics without requiring a symmetry-lowering structural transition. While the Ni $d_{x^2-y^2}$ and d_{z^2} orbitals are energetically distinct, with $d_{x^2-y^2}$ states dominating the in-plane metallic state, we find that d_{z^2} orbitals govern both the interband transition and hopping conduction along the out-of-plane direction. Overall, the unique interplay between the two orbitals in layered nickelates defines the low-energy electrodynamics and yields an emergent quasi-two-dimensional response promoted by DW order. The significant impact of the DW state on the lattice dynamics, in the absence of correspondingly large structural changes, further supports a picture in which the DW state is primarily electronic in origin. Our results imply that any microscopic discussion of the superconducting instability in this family should explicitly account for multiorbital effects and changes of the coupling among the layers.

Note added—After completing this work, we became aware of a recent optical study of trilayer $\text{La}_4\text{Ni}_3\text{O}_{10}$ [75]. While the overall phenomenology is consistent, our work focuses on the effect of the DW transition on the in- and out-of plane electronic response below 100–150 cm^{−1} and the vibrational properties, thereby providing com-

plementary information on the low-energy physics of this material.

We thank D. Nicoletti, J. Li, S. Priya for insightful discussions. Work by Z.G., S.F.R.T., M.T., F.G., C.C.H., M.P.M.D., and M.M. was supported by the U.S. Department of Energy (DOE), Division of Materials Science, under Contract No. DE-SC0012704. Part of the experimental work was performed in the Infrared Lab at the National Synchrotron Light Source II, a DOE Office of Science User Facility operated for the DOE Office of Science by Brookhaven National Laboratory. S.F.R.T. acknowledges additional support from the DOE, Office of Science, Office of Workforce Development for Teachers and Scientists, Office of Science Graduate Student Research (SCGSR) program. The SCGSR program is administered by the Oak Ridge Institute for Science and Education for the DOE under Contract No. DE-SC0014664. A.S.B and Y.Z. acknowledge support from NSF Grant No. DMR-2323971 and the ASU research computing center for HPC resources. Work by X.C. and J.F.M. in the Materials Science Division at Argonne National Laboratory (crystal growth) was supported by the U.S. Department of Energy Office of Science, Basic Energy Sciences, Materials Science and Engineering Division. Work by X.C. and P.K. was supported by AFOSR (FA9550-25-1-0019). A.M.Y. was supported by NSF (DMR-2105048).

* these authors contributed equally

† mmitrano@g.harvard.edu

- [1] Hualei Sun, Mengwu Huo, Xunwu Hu, Jingyuan Li, Zengjia Liu, Yifeng Han, Lingyun Tang, Zhongquan Mao, Pengtao Yang, Bosen Wang, Jinguang Cheng, Dao-Xin Yao, Guang-Ming Zhang, and Meng Wang, “Signatures of superconductivity near 80 K in a nickelate under high pressure,” *Nature* **621**, 493–498 (2023), published online 12 Jul 2023.
- [2] Yanan Zhang, Dajun Su, Yanen Huang, Zhaoyang Shan, Hualei Sun, Mengwu Huo, Kaixin Ye, Jiawen Zhang, Zihan Yang, Yongkang Xu, Yi Su, Rui Li, Michael Smidman, Meng Wang, Lin Jiao, and Huiqiu Yuan, “High-temperature superconductivity with zero resistance and strange-metal behaviour in $\text{La}_3\text{Ni}_2\text{O}_{7-\delta}$,” *Nat. Phys.* **20**, 1269–1273 (2024), published online 6 Jun 2024.
- [3] Yinghao Zhu, Di Peng, Enkang Zhang, Bingying Pan, Xu Chen, Lixing Chen, Huifen Ren, Feiyang Liu, Yiqing Hao, Nana Li, Zhenfang Xing, Fujun Lan, Jiyuan Han, Junjie Wang, Donghan Jia, Hongliang Wo, Yiqing Gu, Yimeng Gu, Li Ji, Wenbin Wang, Huiyang Gou, Yao Shen, Tianping Ying, Xiaolong Chen, Wenge Yang, Huibo Cao, Changlin Zheng, Qiaoshi Zeng, Jian-gang Guo, and Jun Zhao, “Superconductivity in pressurized trilayer $\text{La}_4\text{Ni}_3\text{O}_{10-\delta}$ single crystals,” *Nature* **631**, 531–536 (2024), published 17 Jul 2024.
- [4] Meng Wang, Hai-Hu Wen, Tao Wu, Dao-Xin Yao, and Tao Xiang, “Normal and superconducting properties of $\text{La}_3\text{Ni}_2\text{O}_7$,” *Chin. Phys. Lett.* **41**, 077402 (2024).
- [5] Hirofumi Sakakibara, Masayuki Ochi, Hibiki Nagata,

Yuta Ueki, Hiroya Sakurai, Ryo Matsumoto, Kensei Terashima, Keisuke Hirose, Hiroto Ohta, Masaki Kato, Yoshihiko Takano, and Kazuhiko Kuroki, “Theoretical analysis on the possibility of superconductivity in the trilayer Ruddlesden–Popper nickelate $\text{La}_4\text{Ni}_3\text{O}_{10}$ under pressure and its experimental examination: comparison with $\text{La}_3\text{Ni}_2\text{O}_7$,” *Phys. Rev. B* **109**, 144511 (2024).

[6] Mingxin Zhang, Cuiying Pei, Di Peng, Xian Du, Weixiong Hu, Yantao Cao, Qi Wang, Juefei Wu, Yidian Li, Huanyu Liu, Chenhaoping Wen, Jing Song, Yi Zhao, Changhua Li, Weizheng Cao, Shihao Zhu, Qing Zhang, Na Yu, Peihong Cheng, Lili Zhang, Zhiwei Li, Jinkui Zhao, Yulin Chen, Changqing Jin, Hanjie Guo, Congjun Wu, Fan Yang, Qiaoshi Zeng, Shichao Yan, Lexian Yang, and Yanpeng Qi, “Superconductivity in trilayer nickelate $\text{La}_4\text{Ni}_3\text{O}_{10}$ under pressure,” *Phys. Rev. X* **15**, 021005 (2025).

[7] Qing Li, Ying-Jie Zhang, Zhe-Ning Xiang, Yuhang Zhang, Xiyu Zhu, and Hai-Hu Wen, “Signature of superconductivity in pressurized $\text{La}_4\text{Ni}_3\text{O}_{10}$,” *Chin. Phys. Lett.* **41**, 017401 (2024).

[8] Pascal Puphal, Thomas Schäfer, Bernhard Keimer, and Matthias Hepting, “Superconductivity in infinite-layer and Ruddlesden–Popper nickelates,” *Nat. Rev. Phys.* (2025), 10.1038/s42254-025-00898-2, published online 12 Dec 2025.

[9] Yuxin Wang, Kun Jiang, Jianjun Ying, Tao Wu, Jinguang Cheng, Jiangping Hu, and Xianhui Chen, “Recent progress in nickelate superconductors,” *Natl. Sci. Rev.* **12**, nwaf373 (2025).

[10] Kaiwen Chen, Xiangqi Liu, Jiachen Jiao, Muyuan Zou, Chengyu Jiang, Xin Li, Yixuan Luo, Qiong Wu, Ningyuan Zhang, Yanfeng Guo, and Lei Shu, “Evidence of spin density waves in $\text{La}_3\text{Ni}_2\text{O}_{7-\delta}$,” *Phys. Rev. Lett.* **132**, 256503 (2024).

[11] Tao Xie, Mengwu Huo, Xiaosheng Ni, Feiran Shen, Xing Huang, Hualei Sun, Helen C. Walker, Devashibhai Adroja, Dehong Yu, Bing Shen, Lunhua He, Kun Cao, and Meng Wang, “Strong interlayer magnetic exchange coupling in $\text{La}_3\text{Ni}_2\text{O}_{7-\delta}$ revealed by inelastic neutron scattering,” *Sci. Bull.* **69**, 3221–3227 (2024).

[12] Rustem Khasanov, Thomas J. Hicken, Dariusz J. Gawryluk, Vahid Sazgari, Igor Plokhikh, Loïc Pierre Sorel, Marek Bartkowiak, Steffen Böttzel, Frank Lechermann, Ilya M. Eremin, Hubertus Luetkens, and Zurab Guguchia, “Pressure-enhanced splitting of density wave transitions in $\text{La}_3\text{Ni}_2\text{O}_{7-\delta}$,” *Nat. Phys.* **21**, 430–436 (2025).

[13] Junjie Zhang, D. Phelan, A. S. Botana, Yu-Sheng Chen, Hong Zheng, M. Krogstad, Suyin Grass Wang, Yiming Qiu, J. A. Rodriguez-Rivera, R. Osborn, S. Rosenkranz, M. R. Norman, and J. F. Mitchell, “Intertwined density waves in a metallic nickelate,” *Nat. Commun.* **11**, 6003 (2020).

[14] Rustem Khasanov, Thomas J. Hicken, Igor Plokhikh, Vahid Sazgari, Lukas Keller, Vladimir Pomjakushin, Marek Bartkowiak, Szymon Królak, Michał J. Winiarski, Jonas A. Krieger, Hubertus Luetkens, Tomasz Klimczuk, Dariusz J. Gawryluk, and Zurab Guguchia, “Identical suppression of spin and charge density wave transitions in $\text{La}_4\text{Ni}_3\text{O}_{10}$ by pressure,” (2025), arXiv:2503.04400 [cond-mat.supr-con].

[15] Shuxiang Xu, Hao Wang, Mengwu Huo, Deyuan Hu, Qiong Wu, Li Yue, Dong Wu, Meng Wang, Tao Dong, and Nanlin Wang, “Collapse of density wave and emergence of superconductivity in pressurized $\text{La}_4\text{Ni}_3\text{O}_{10}$ evidenced by ultrafast spectroscopy,” *Nat. Commun.* **16**, 7039 (2025).

[16] Dong-Hyeon Gim, Chung Ha Park, and Kee Hoon Kim, “Orbital-selective quasiparticle depletion across the density wave transition in trilayer nickelate $\text{La}_4\text{Ni}_3\text{O}_{10}$,” *Phys. Rev. Lett.* **135**, 136505 (2025).

[17] Ming Zhang, Hongyi Sun, Yu-Bo Liu, Qihang Liu, Wei-Qiang Chen, and Fan Yang, “Spin-density wave and superconductivity in $\text{La}_4\text{Ni}_3\text{O}_{10}$ under ambient pressure,” *Phys. Rev. B* **111**, 144502 (2025).

[18] Cui-Qun Chen, Zhihui Luo, Meng Wang, Wéi Wú, and Dao-Xin Yao, “Trilayer multiorbital models of $\text{La}_4\text{Ni}_3\text{O}_{10}$,” *Phys. Rev. B* **110**, 014503 (2024).

[19] Qing-Geng Yang, Kai-Yue Jiang, Da Wang, Hong-Yan Lu, and Qiang-Hua Wang, “Effective model and s_{\pm} -wave superconductivity in trilayer nickelate $\text{La}_4\text{Ni}_3\text{O}_{10}$,” *Phys. Rev. B* **109**, L220506 (2024).

[20] Yang Zhang, Ling-Fang Lin, Adriana Moreo, Thomas A. Maier, and Elbio Dagotto, “Prediction of s_{\pm} -wave superconductivity enhanced by electronic doping in trilayer nickelates $\text{La}_4\text{Ni}_3\text{O}_{10}$ under pressure,” *Phys. Rev. Lett.* **133**, 136001 (2024).

[21] Harrison LaBollita, Jesse Kapeghian, Michael R. Norman, and Antia S. Botana, “Electronic structure and magnetic tendencies of trilayer $\text{La}_4\text{Ni}_3\text{O}_{10}$ under pressure: Structural transition, molecular orbitals, and layer differentiation,” *Phys. Rev. B* **109**, 195151 (2024).

[22] I. V. Leonov, “Electronic structure and magnetic correlations in the trilayer nickelate superconductor $\text{La}_4\text{Ni}_3\text{O}_{10}$ under pressure,” *Phys. Rev. B* **109**, 235123 (2024).

[23] Peng-Fei Tian, Hao-Tian Ma, Xing Ming, Xiao-Jun Zheng, and Huan Li, “Effective model and electron correlations in trilayer nickelate superconductor $\text{La}_4\text{Ni}_3\text{O}_{10}$,” *J. Phys.: Condens. Matter* **36**, 355602 (2024).

[24] Junkang Huang and Tao Zhou, “Interlayer pairing-induced partially gapped Fermi surface in trilayer $\text{La}_4\text{Ni}_3\text{O}_{10}$ superconductors,” *Phys. Rev. B* **110**, L060506 (2024).

[25] Jing-Xuan Wang, Zhenfeng Ouyang, Rong-Qiang He, and Zhong-Yi Lu, “Non-Fermi liquid and Hund correlation in $\text{La}_4\text{Ni}_3\text{O}_{10}$ under high pressure,” *Phys. Rev. B* **109**, 165140 (2024).

[26] “See supplemental material at for details on sample preparation, optical measurements, drude–lorentz analysis, and dft calculations of the optical response, extraction of the density wave gap, electronic correlation calculation, transport resistivity measurements, and analysis of phonon modes.” Supplemental Material (2026).

[27] D. N. Basov and T. Timusk, “Electrodynamics of high- T_c superconductors,” *Rev. Mod. Phys.* **77**, 721–779 (2005).

[28] Martin Dressel and George Grüner, *Electrodynamics of solids: optical properties of electrons in matter* (Cambridge University Press, 2002).

[29] D. B. Tanner, “Use of x-ray scattering functions in Kramers–Kronig analysis of reflectance,” *Phys. Rev. B* **91**, 035123 (2015).

[30] S. Uchida, K. Tamasaku, and S. Tajima, “ c -axis optical spectra and charge dynamics in $\text{La}_{2-x}\text{Sr}_x\text{CuO}_4$,” *Phys. Rev. B* **53**, 14558–14574 (1996).

[31] C. C. Homes, T. Timusk, D. A. Bonn, R. Liang, and W. N. Hardy, “Optical properties along the c -axis of $\text{YBa}_2\text{Cu}_3\text{O}_{6+x}$, for $x = 0.50$ –0.95: evolution of the

pseudogap,” *Physica C: Superconductivity* **254**, 265–280 (1995).

[32] S. L. Cooper, D. Reznik, A. Kotz, M. A. Karlow, R. Liu, M. V. Klein, W. C. Lee, J. Giapintzakis, D. M. Ginsberg, B. W. Veal, and A. P. Paulikas, “Optical studies of the *a*-, *b*-, and *c*-axis charge dynamics in $\text{YBa}_2\text{Cu}_3\text{O}_{6+x}$,” *Phys. Rev. B* **47**, 8233–8248 (1993).

[33] J. Schützmann, S. Tajima, S. Miyamoto, and S. Tanaka, “*c*-axis optical response of fully oxygenated $\text{YBa}_2\text{Cu}_3\text{O}_{7-\delta}$: observation of dirty-limit-like superconductivity and residual unpaired carriers,” *Phys. Rev. Lett.* **73**, 174–177 (1994).

[34] Z. G. Chen, T. Dong, R. H. Ruan, B. F. Hu, B. Cheng, W. Z. Hu, P. Zheng, Z. Fang, X. Dai, and N. L. Wang, “Measurement of the *c*-axis optical reflectance of $A\text{Fe}_2\text{As}_2$ ($A = \text{Ba}, \text{Sr}$) single crystals: Evidence of different mechanisms for the formation of two energy gaps,” *Phys. Rev. Lett.* **105**, 097003 (2010).

[35] B. Cheng, Z. G. Chen, C. L. Zhang, R. H. Ruan, T. Dong, B. F. Hu, W. T. Guo, S. S. Miao, P. Zheng, J. L. Luo, G. Xu, Pengcheng Dai, and N. L. Wang, “Three-dimensionality of band structure and a large residual quasiparticle population in $\text{Ba}_{0.67}\text{K}_{0.33}\text{Fe}_2\text{As}_2$ as revealed by *c*-axis polarized optical measurements,” *Phys. Rev. B* **83**, 144522 (2011).

[36] S. J. Moon, C. C. Homes, A. Akrap, Z. J. Xu, J. S. Wen, Z. W. Lin, Q. Li, G. D. Gu, and D. N. Basov, “Incoherent *c*-axis interplane response of the iron chalcogenide $\text{FeTe}_{0.55}\text{Se}_{0.45}$ superconductor from infrared spectroscopy,” *Phys. Rev. Lett.* **106**, 217001 (2011).

[37] S. J. Moon, A. A. Schafgans, M. A. Tanatar, R. Prozorov, A. Thaler, P. C. Canfield, A. S. Sefat, D. Mandrus, and D. N. Basov, “Interlayer coherence and superconducting condensate in the *c*-axis response of optimally doped $\text{Ba}(\text{Fe}_{1-x}\text{Co}_x)_2\text{As}_2$ high- T_c superconductor using infrared spectroscopy,” *Phys. Rev. Lett.* **110**, 097003 (2013).

[38] S. Shinomori, M. Kawasaki, and Y. Tokura, “Orientation-controlled epitaxy and anisotropic properties of $\text{La}_{2-x}\text{Sr}_x\text{NiO}_4$ with $0.5 \leq x \leq 1.5$ covering the insulator–metal transition,” *Appl. Phys. Lett.* **80**, 574–576 (2002).

[39] Benjamin Geisler, Laura Fanfarillo, James J. Hamlin, Gregory R. Stewart, Richard G. Hennig, and P. J. Hirschfeld, “Optical properties and electronic correlations in $\text{La}_3\text{Ni}_2\text{O}_7$ bilayer nickelates under high pressure,” *npj Quantum Mater.* **9**, 89 (2024).

[40] Zhe Liu, Mengwu Huo, Jie Li, Qing Li, Yuecong Liu, Yaomin Dai, Xiaoxiang Zhou, Jiahao Hao, Yi Lu, Meng Wang, and Hai-Hu Wen, “Electronic correlations and partial gap in the bilayer nickelate $\text{La}_3\text{Ni}_2\text{O}_7$,” *Nat. Commun.* **15**, 7570 (2024).

[41] Shuxiang Xu, Cui-Qun Chen, Mengwu Huo, Deyuan Hu, Hao Wang, Qiong Wu, Rongsheng Li, Dong Wu, Meng Wang, Dao-Xin Yao, Tao Dong, and Nanlin Wang, “Origin of the density wave instability in trilayer nickelate $\text{La}_4\text{Ni}_3\text{O}_{10}$ revealed by optical and ultrafast spectroscopy,” *Phys. Rev. B* **111**, 075140 (2025).

[42] Mingzhe Li, Jiashuo Gong, Yinghao Zhu, Ziyuan Chen, Jiakang Zhang, Enkang Zhang, Yuanji Li, Ruotong Yin, Shiyuan Wang, Jun Zhao, Dong-Lai Feng, Zengyi Du, and Ya-Jun Yan, “Direct visualization of an incommensurate unidirectional charge density wave in $\text{La}_4\text{Ni}_3\text{O}_{10}$,” *Phys. Rev. B* **112**, 045132 (2025).

[43] A. Suthar, V. Sundaramurthy, M. Bejas, Congcong Le, P. Puphal, P. Sosa-Lizama, A. Schulz, J. Nuss, M. Isobe, P. A. van Aken, Y. E. Suyolcu, M. Minola, A. P. Schnyder, Xianxin Wu, B. Keimer, G. Khaliullin, A. Greco, and M. Hepting, “Multiorbital character of the density wave instability in $\text{La}_4\text{Ni}_3\text{O}_{10}$,” (2025), arXiv:2508.06440 [cond-mat.str-el].

[44] M. R. Norman, “Landau theory of the density wave transition in trilayer Ruddlesden-Popper nickelates,” *Phys. Rev. B* **112**, 075149 (2025).

[45] Junjie Zhang, Hong Zheng, Yu-Sheng Chen, Yang Ren, Masao Yonemura, Ashfia Huq, and J. F. Mitchell, “High oxygen pressure floating zone growth and crystal structure of the metallic nickelates $R_4\text{Ni}_3\text{O}_{10}$ ($R = \text{La}, \text{Pr}$),” *Phys. Rev. Mater.* **4**, 083402 (2020).

[46] Victor Pardo and Warren E. Pickett, “Quantum confinement induced molecular correlated insulating state in $\text{La}_4\text{Ni}_3\text{O}_8$,” *Phys. Rev. Lett.* **105**, 266402 (2010).

[47] Myung-Chul Jung, Jesse Kapeghian, Chase Hanson, Betül Pamuk, and Antia S. Botana, “Electronic structure of higher-order Ruddlesden-Popper nickelates,” *Phys. Rev. B* **105**, 085150 (2022).

[48] Binhua Zhang, Changsong Xu, and Hongjun Xiang, “Spin-charge-orbital order in nickelate superconductors,” *Phys. Rev. B* **111**, 184401 (2025).

[49] Zhe Liu, Jie Li, Mengwu Huo, Bingke Ji, Jiahao Hao, Yaomin Dai, Mengjun Ou, Qing Li, Hualei Sun, Bing Xu, Yi Lu, Meng Wang, and Hai-Hu Wen, “Evolution of electronic correlations in the Ruddlesden-Popper nickelates,” *Phys. Rev. B* **111**, L220505 (2025).

[50] Bo Su, Chaoxin Huang, Jianzhou Zhao, Mengwu Huo, Jianlin Luo, Meng Wang, and Zhi-Guo Chen, “Strongly anisotropic charge dynamics in $\text{La}_3\text{Ni}_2\text{O}_7$ with coherent-to-incoherent crossover of interlayer charge dynamics,” (2024), arXiv:2411.10786 [cond-mat.supr-con].

[51] Haoxiang Li, Xiaoqing Zhou, Thomas Nummy, Junjie Zhang, Victor Pardo, Warren E. Pickett, J. F. Mitchell, and D. S. Dessau, “Fermiology and electron dynamics of trilayer nickelate $\text{La}_4\text{Ni}_3\text{O}_{10}$,” *Nat. Commun.* **8**, 704 (2017).

[52] Y. Nakamura and S. Uchida, “Anisotropic transport properties of single-crystal $\text{La}_{2-x}\text{Sr}_x\text{CuO}_4$: Evidence for the dimensional crossover,” *Phys. Rev. B* **47**, 8369–8372 (1993).

[53] Seiki Komiya, Yoichi Ando, X. F. Sun, and A. N. Lavrov, “*c*-axis transport and resistivity anisotropy of lightly to moderately doped $\text{La}_{2-x}\text{Sr}_x\text{CuO}_4$ single crystals: Implications on the charge transport mechanism,” *Phys. Rev. B* **65**, 214535 (2002).

[54] S. Martin, A. T. Fiory, R. M. Fleming, L. F. Schneemeyer, and J. V. Waszczak, “Temperature dependence of the resistivity tensor in superconducting $\text{Bi}_2\text{Sr}_{2.2}\text{Ca}_{0.8}\text{Cu}_2\text{O}_8$ crystals,” *Phys. Rev. Lett.* **60**, 2194–2197 (1988).

[55] T. Watanabe, T. Fujii, and A. Matsuda, “Anisotropic resistivities of precisely oxygen controlled single-crystal $\text{Bi}_2\text{Sr}_2\text{CaCu}_2\text{O}_{8+\delta}$: systematic study on “spin gap” effect,” *Phys. Rev. Lett.* **79**, 2113–2116 (1997).

[56] V. N. Zavaritsky and A. S. Alexandrov, “Normal state of extremely anisotropic superconducting cuprates as revealed by magnetotransport,” *Phys. Rev. B* **71**, 012502 (2005).

[57] K. Takenaka, K. Mizuhashi, H. Takagi, and S. Uchida, “Interplane charge transport in $\text{YBa}_2\text{Cu}_3\text{O}_{7-y}$: spin-

gap effect on in-plane and out-of-plane resistivity," Phys. Rev. B **50**, 6534–6537 (1994).

[58] N. E. Hussey, K. Nozawa, H. Takagi, S. Adachi, and K. Tanabe, "Anisotropic resistivity of $\text{YBa}_2\text{Cu}_4\text{O}_8$: Incoherent-to-metallic crossover in the out-of-plane transport," Phys. Rev. B **56**, R11423–R11426 (1997).

[59] A. N. Lavrov, M. Yu. Kameneva, and L. P. Kozeleva, "Normal-state resistivity anisotropy in under-doped $\text{RBa}_2\text{Cu}_3\text{O}_{6+x}$ crystals," Phys. Rev. Lett. **81**, 5636–5639 (1998).

[60] X. F. Wang, T. Wu, G. Wu, H. Chen, Y. L. Xie, J. J. Ying, Y. J. Yan, R. H. Liu, and X. H. Chen, "Anisotropy in the electrical resistivity and susceptibility of superconducting BaFe_2As_2 single crystals," Phys. Rev. Lett. **102**, 117005 (2009).

[61] G. F. Chen, Z. Li, J. Dong, G. Li, W. Z. Hu, X. D. Zhang, X. H. Song, P. Zheng, N. L. Wang, and J. L. Luo, "Transport and anisotropy in single-crystalline SrFe_2As_2 and $\text{A}_{0.6}\text{K}_{0.4}\text{Fe}_2\text{As}_2$ ($\text{A} = \text{Sr, Ba}$) superconductors," Phys. Rev. B **78**, 224512 (2008).

[62] M. A. Tanatar, N. Ni, G. D. Samolyuk, S. L. Bud'ko, P. C. Canfield, and R. Prozorov, "Resistivity anisotropy of AFe_2As_2 ($\text{A} = \text{Ca, Sr, Ba}$): direct versus Montgomery technique measurements," Phys. Rev. B **79**, 134528 (2009).

[63] M. Nakajima, M. Nagafuchi, and S. Tajima, "Comprehensive study of out-of-plane transport properties in BaFe_2As_2 : three-dimensional electronic state and effect of chemical substitution," Phys. Rev. B **97**, 094511 (2018).

[64] Hang-Dong Wang, Chi-Heng Dong, Zu-Juan Li, Qian-Hui Mao, Sha-Sha Zhu, Chun-Mu Feng, H. Q. Yuan, and Ming-Hu Fang, "Superconductivity at 32 K and anisotropy in $\text{Tl}_{0.58}\text{Rb}_{0.42}\text{Fe}_{1.72}\text{Se}_2$ crystals," Europhys. Lett. **93**, 47004 (2011).

[65] Hechang Lei and C. Petrovic, "Anisotropy in transport and magnetic properties of $\text{K}_{0.64}\text{Fe}_{1.44}\text{Se}_2$," Phys. Rev. B **83**, 184504 (2011).

[66] S. I. Vedeneev, B. A. Piot, D. K. Maude, and A. V. Sadakov, "Temperature dependence of the upper critical field of FeSe single crystals," Phys. Rev. B **87**, 134512 (2013).

[67] Yoo Jang Song, Jin Soo Ghim, Byeong Hun Min, Yong Seung Kwon, Myung Hwa Jung, and Jong-Soo Rhyee, "Synthesis, anisotropy, and superconducting properties of LiFeAs single crystal," Appl. Phys. Lett. **96**, 212508 (2010).

[68] Zhuoyu Chen and Haoliang Huang, "The nickelate bridge between cuprate and iron-based superconductivity," Quantum Front. **4**, 17 (2025).

[69] Susmit Kumar, Øystein Fjellvåg, Anja Olafsen Sjåstad, and Helmer Fjellvåg, "Physical properties of Ruddlesden-Popper ($n = 3$) nickelate: $\text{La}_4\text{Ni}_3\text{O}_{10}$," Journal of Magnetism and Magnetic Materials **496**, 165915 (2020).

[70] Dibyata Rout, Sancharita Ranajit Mudi, Marco Hoffmann, Sven Spachmann, Rüdiger Klingeler, and Surjeet Singh, "Structural and physical properties of trilayer nickelates $\text{R}_4\text{Ni}_3\text{O}_{10}$ ($\text{R} = \text{La, Pr, Nd}$)," Phys. Rev. B **102**, 195144 (2020).

[71] Nana Li, Jiayi Guan, Limin Yan, Xiaozhi Yan, Mingtao Li, Xuqiang Liu, Kai Zhang, Feiyu Li, Shu Cai, Haini Dong, Adama N-Diaye, Monica Amboage, Junjie Zhang, Yantao Cao, Hanjie Guo, Qingyu Kong, Liling Sun, and Wenge Yang, "Crystal and electronic structure studies of $\text{La}_4\text{Ni}_3\text{O}_{10-\delta}$ under high-pressure and low-temperature conditions," J. Am. Chem. Soc. **147**, 43717–43726 (2025).

[72] Sonia Deswal, Deepu Kumar, Dibyata Rout, Surjeet Singh, and Pradeep Kumar, "Dynamics of electron-electron correlation and electron-phonon coupled phase progression in trilayer nickelate $\text{La}_4\text{Ni}_3\text{O}_{10}$," Appl. Phys. Lett. **127**, 071903 (2025).

[73] Dipankar Jana, Diana Vaclavkova, Rajesh Kumar Ulaganathan, Raman Sankar, Milan Orlita, Clement Faugeras, Maciej Koperski, M. E. Zhitomirsky, and Marek Potemski, "Strong and selective magnon-phonon coupling in the van der Waals antiferromagnet CoPS_3 ," Phys. Rev. B **112**, 165427 (2025).

[74] Xiaoyang Chen, Jaewon Choi, Zhicheng Jiang, Jiong Mei, Kun Jiang, Jie Li, Stefano Agrestini, Mirian Garcia-Fernandez, Hualei Sun, Xing Huang, Dawei Shen, Meng Wang, Jiangping Hu, Yi Lu, Ke-Jin Zhou, and Donglai Feng, "Electronic and magnetic excitations in $\text{La}_3\text{Ni}_2\text{O}_7$," Nat. Commun. **15**, 9597 (2024).

[75] Zhe Liu, Jie Li, Deyuan Hu, Bingke Ji, Haoran Zhang, Jiahao Hao, Yaomin Dai, Qing Li, Mengjun Ou, Bing Xu, Yi Lu, Meng Wang, and Hai-Hu Wen, "Highly anisotropic charge dynamics and spectral weight redistribution in the trilayer nickelate $\text{La}_4\text{Ni}_3\text{O}_{10}$," (2025), arXiv:2512.03806 [cond-mat.supr-con].

Supplemental Material for: Electronic layer decoupling driven by density-wave order in $\text{La}_4\text{Ni}_3\text{O}_{10}$

Ziqiang Guan,¹ Sophia F. R. TenHuisen,^{1,2} M. Tepie,¹ Yifeng Zhao,³ Ezra Day-Roberts,³ Harrison LaBollita,³ Alexander M. Young,¹ Xiaomeng Cui,¹ Xinglong Chen,⁴ Filippo Glerean,^{1,5} Carl Audric Guia,¹ Mark P. M. Dean,⁵ Philip Kim,^{1,2} J. F. Mitchell,⁴ Antia S. Botana,³ Christopher C. Homes,⁶ and Matteo Mitrano¹

¹*Department of Physics, Harvard University, Cambridge, Massachusetts 02138, USA*

²*John A. Paulson School of Engineering and Applied Sciences,
Harvard University, Cambridge, Massachusetts 02138, USA*

³*Department of Physics, Arizona State University, Tempe, Arizona 85287, USA*

⁴*Materials Science Division, Argonne National Laboratory, Lemont, Illinois 60439, USA*

⁵*Condensed Matter Physics and Materials Science Department,
Brookhaven National Laboratory, Upton, New York 11973, USA*

⁶*National Synchrotron Light Source II, Brookhaven National Laboratory, Upton, NY, USA*

(Dated: January 15, 2026)

S1. SAMPLE PREPARATION, OPTICAL EXPERIMENTAL METHODS, AND FULL TEMPERATURE-DEPENDENT DATASET

High-quality single crystals of $\text{La}_4\text{Ni}_3\text{O}_{10}$ were grown using a vertical optical-image floating zone furnace operating at high O_2 pressure according to the procedures described in Ref.¹. The quality and orientation of the single crystals were confirmed by x-ray Laue diffraction. Two large single crystals (approximately $3 \times 2 \times 2 \text{ mm}^3$) of $\text{La}_4\text{Ni}_3\text{O}_{10}$ were polished to expose an ab -plane and an ac^* -plane, respectively. The near-normal-incidence reflectivity $R(\omega)$ at ambient pressure was measured in the frequency range of $60\text{--}22,000 \text{ cm}^{-1}$ using a Bruker Vertex 80v Fourier-transform infrared spectrometer (FTIR) and referenced with *in situ* gold evaporation².

We used unpolarized light to measure the ab -plane reflectivity on an ab -plane-polished sample. Polishing introduced a small misorientation of the crystal surface ($\sim 2^\circ$), as verified by subsequent x-ray diffraction on the same sample. This misorientation slightly mixes c^* -axis signatures into the ab -plane FTIR measurement with unpolarized light, which in practice appears as a small reduction of the overall reflectivity and weak phonon-like peaks at the same frequencies as in the c^* -axis spectrum³. We correct for this mixing by subtracting the c^* -axis reflectivity contribution and renormalizing the result. This correction does not affect the conclusions of this article. Owing to the high ab -plane conductivity and reflectivity, we use a Hagen-Rubens extrapolation below the lowest measured frequency.

We used out-of-plane-polarized light to measure the c^* -axis reflectivity on an ac^* -plane-polished sample. For this configuration, we also performed polarization-resolved terahertz time-domain spectroscopy (THz-TDS) to extend the low-frequency data down to 30 cm^{-1} . We employed an echelon-based single-shot THz-TDS system^{4,5} pumped by 800 nm, 35 fs pulses from a 1 kHz Ti:sapphire amplifier. THz pulses were generated in a 0.5-mm-thick $\langle 110 \rangle$ ZnTe crystal and electro-optic sampling of the light reflected from the sample was carried out focusing on a 0.2-mm-thick $\langle 110 \rangle$ ZnTe sensor optically contacted to a 1-mm-thick $\langle 100 \rangle$ ZnTe substrate. The THz reflectivity was obtained by normalizing the THz spectrum of the sample to that of a gold reference measured under identical conditions. The entire THz-TDS apparatus operated under vacuum. Because the c^* -axis conductivity and reflectivity are lower and the low-frequency region contains many Lorentz modes, we fit the low-frequency reflectivity with a Drude model including a background dielectric permittivity (a simple $\varepsilon_\infty + \text{Drude}$ approximation) and use it to extrapolate below the lowest measured frequency⁶.

The complex optical conductivity was determined via a Kramers-Kronig analysis of the measured reflectivity. For both the ab -plane and c^* -axis reflectivity, we use an x-ray atomic scattering factor for the high-frequency extrapolation⁶. We also tested different high-frequency extrapolation methods, such as assuming a constant reflectivity up to 10^6 cm^{-1} ($\sim 124 \text{ eV}$) followed by a free-electron (ω^{-4}) response. The complex optical conductivity calculated based on different methods shows no qualitative difference in the measured frequency range.

Fig. S1 shows the full temperature-dependent reflectivity and conductivity data set of both in-plane and out-of-plane polarization. The ab -plane response shows robust metallic behavior as the reflectivity approaches unity in the zero-frequency limit and keeps rising with decreasing temperature in the far-infrared range ($< 400 \text{ cm}^{-1}$). Suppression in the mid-infrared range ($400\text{--}1000 \text{ cm}^{-1}$), together with the spectral weight transfer to higher frequency range, indicate the onset of a density wave energy gap below the transition temperature of 140 K. For the out-of-plane response, the low frequency ($< 100 \text{ cm}^{-1}$) reflectivity shows an upturn for temperatures above the DW transition, suggesting a finite Drude component. However, the Drude component is suppressed at low temperatures and remains relatively small compared to the Lorentzian phonon modes or the interband transitions as seen in the conductivity.

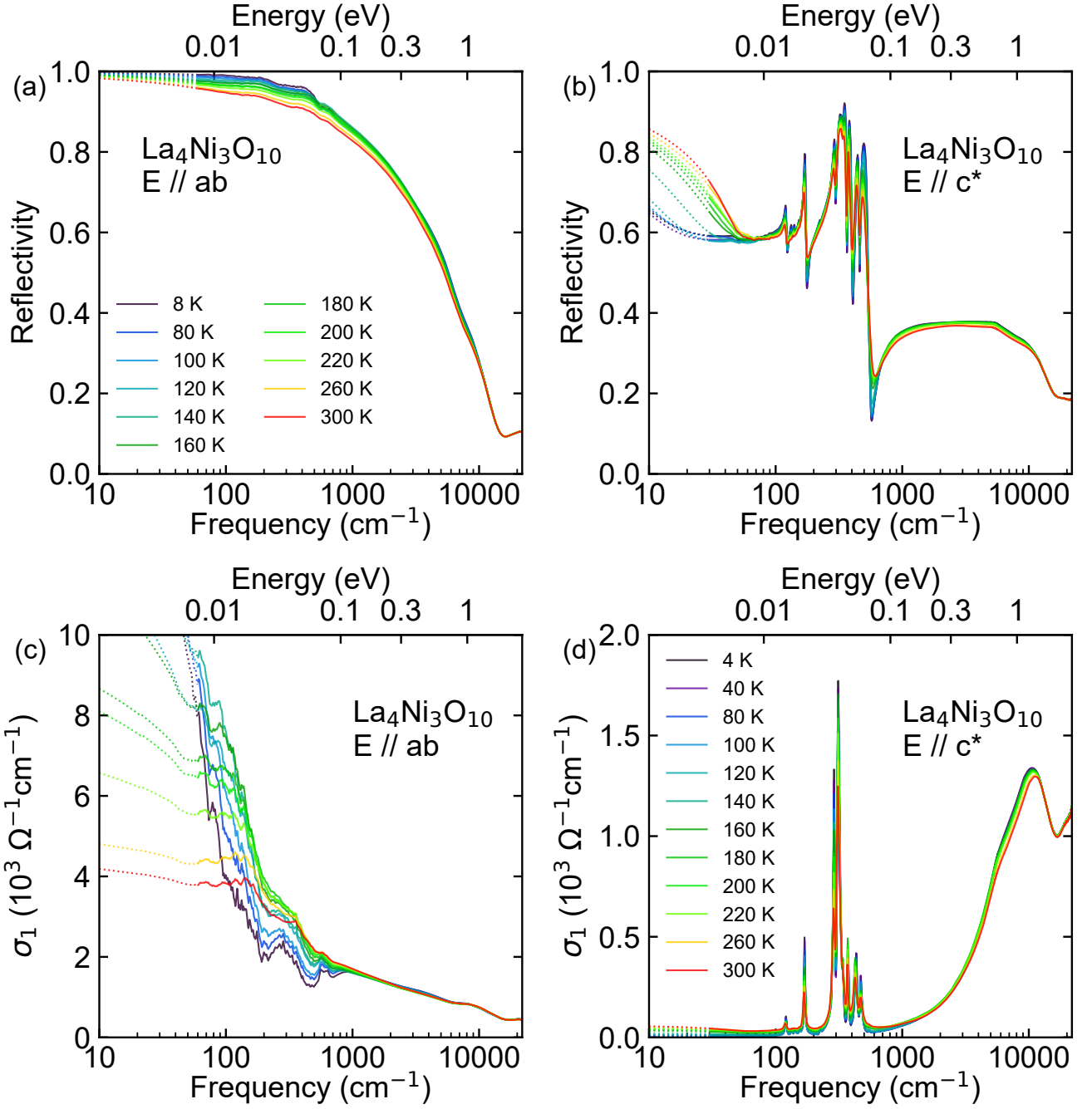


FIG. S1. Reflectivity (a)(b) and real part of optical conductivity (c)(d) over a broad frequency at all measured temperatures. Out-of-plane ($E \parallel c^*$) and in-plane ($E \parallel ab$) are shown on the left and right, respectively. Dotted lines indicate the low-frequency extrapolations as described in experimental method Sec. S1.

S2. DFT ELECTRONIC STRUCTURE AND OPTICAL PROPERTIES

The electronic structure and optical properties calculations were performed using all-electron, full-potential DFT code WIEN2K⁷. We used the Perdew-Burke-Ernzerhof version of the generalized gradient approximation as the exchange-correlation functional⁸. All calculations were performed using the experimental structure with $P2_1/a$ symmetry at ambient pressure¹ in the nonmagnetic state. A $5 \times 13 \times 13$ k-point grid was used for the Brillouin sampling

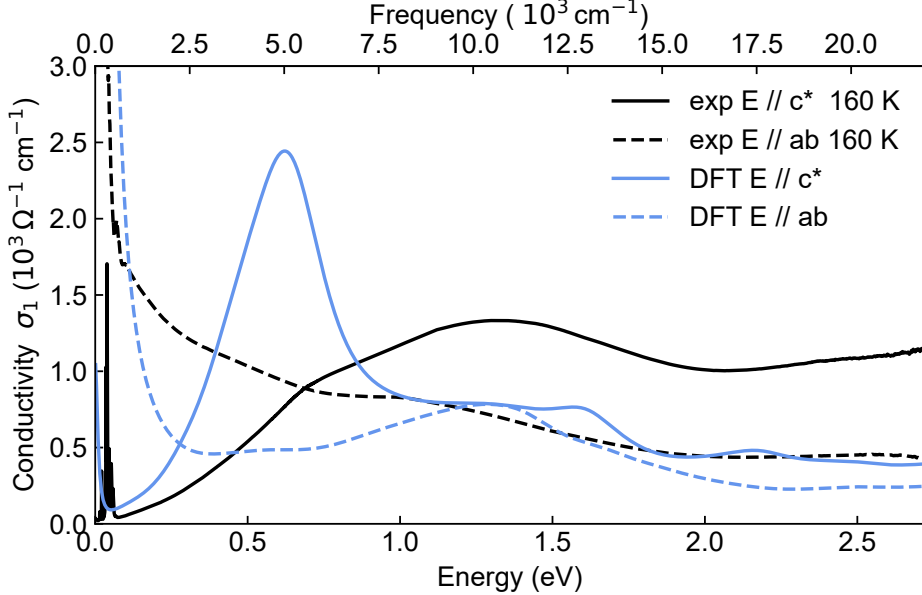


FIG. S2. Comparison of optical conductivity measured experimentally (exp) and calculated with DFT.

in self-consistent calculations, while a denser k -point grid of $11 \times 29 \times 30$ was used to accurately describe the optical properties. An $RK_{\max} = 7$ and muffin-tin radii of 2.38, 1.91, and 1.70 a.u. were used for La, Ni, O, respectively. The broadening factor (scattering rate) used to compute the interband contribution to the optical conductivity is set to be 0.1 eV. For the intraband contribution, the plasma frequency is directly obtained from DFT calculations, while the scattering rate (Drude width) is taken from fitted parameters in the experimental optical conductivity $\sigma(\omega)$ at 160 K. The in-plane optical conductivity is obtained by averaging the two inequivalent in-plane components.

Figure. S2 presents the comparison between experimentally measured and DFT calculated real part of the optical conductivity. The DFT calculation shown here did not include a Hubbard U . Similarly to the experimental result, the DFT calculation also reveals a strong anisotropy reversal as a function of frequency. The DFT calculated out-of-plane optical conductivity exceeds the in-plane components substantially around 0.6 eV. However, the anisotropy crossover appears near 0.3 eV, much lower than the experimentally observed crossover energy. This discrepancy is to some extent expected as general DFT calculations usually underestimate the interband transition energies⁹. Electronic-correlation-induced mass-renormalization could also contribute to the underestimation of the interband transition energy, as suggested by previous ARPES results¹⁰. Further, the calculations were performed in the nonmagnetic state only and not in the DW state (where the Ni-O planes are decoupled via the nonmagnetic mirror layer).

Next, we analyze the orbital contribution to the anisotropic optical conductivity. Figure. S3 shows the DFT calculated band structure with Hubbard $U = 0$. Near the Fermi level, Ni $d_{x^2-y^2}$ and d_{z^2} bands dominates the optical transitions. By comparing the band structure with the optical conductivity, we identify that the main contributions to the in-plane interband conductivity arise from transitions between bands with dominant $d_{x^2-y^2}$ character, while the out-of-plane interband conductivity is mainly associated with transitions between bands of dominant d_{z^2} character. This orbital dependence of the optical conductivity can be understood from the spatial orientation of the two $3d$ orbitals of the Ni atom. The $d_{x^2-y^2}$ orbitals lie in the Ni-O plane and mainly contribute to electronic coupling within the plane, while the d_{z^2} orbitals extend along the c^* -axis and mainly contribute to the charge transport between layers. The difference in the orbital orientations naturally leads to the strong polarization dependence in the optical response.

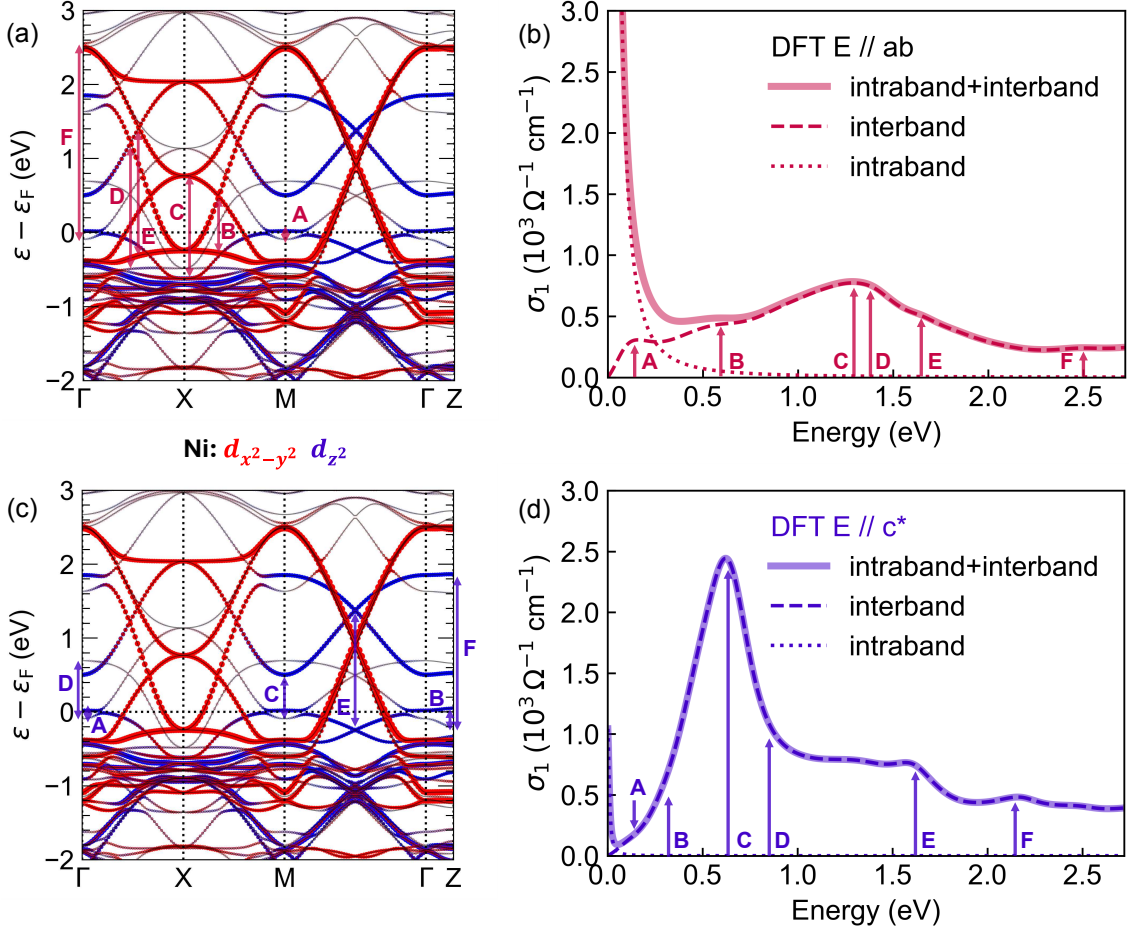


FIG. S3. DFT calculated band structure and optical conductivity of $\text{La}_4\text{Ni}_3\text{O}_{10}$. Panels (a) and (c) display identical band structures, colored to highlight the dominant orbital character: Ni $d_{x^2-y^2}$ components in red and d_{z^2} components in blue. These bands give rise to the distinct optical conductivities along the in-plane and out-of-plane directions, shown in (b) and (d), respectively. The total optical conductivity, along with its interband and intraband components, is presented for both polarizations. The arrows in (b) and (d) indicate the principal optical transitions, corresponding to the interband processes labeled in the band structures. The Fermi level is set to be 0 eV in panels (a) and (c).

S3. DENSITY WAVE ENERGY GAP EXTRACTION

The DW optical gap appears in the in-plane conductivity as a transfer of spectral weight from low to higher frequencies. We extract the gap by analyzing the conductivity difference spectrum, $\Delta\sigma_1(\omega) = \sigma_1(\omega, T < T_{\text{DW}}) - \sigma_1(\omega, T_{\text{DW}})$. We take the spectrum just above the DW transition (140 K) as the normal-state reference to minimize unrelated temperature-dependent effects.

Fig. S4(a) compares the in-plane optical conductivities at 8 K and 140 K. The spectra show a suppression in the mid-infrared and an enhancement at higher frequencies, crossing near 1000 cm^{-1} . We attribute this spectral-weight transfer to the opening of the DW gap, since a simple narrowing of the Drude peak cannot account for the high-frequency enhancement. Fig. S4(b) shows the 8 K difference conductivity $\Delta\sigma_1(\omega)$; the zero-crossing point (black arrow) defines the optical gap, $2\Delta = 112 \text{ meV}$. The resulting DW gap, $\Delta = 56 \text{ meV}$, agrees with a previous FTIR report on the same material (61 meV)¹¹. For $T_{\text{DW}} = 140 \text{ K}$, this yields $2\Delta/k_B T_{\text{DW}} \approx 9.3$, far above the weak-coupling value of 3.52, highlighting the unconventional nature of the DW transition in $\text{La}_4\text{Ni}_3\text{O}_{10}$.

The temperature dependence of energy gap Δ [Fig. S4(c)] follows a mean-field behavior. We obtain the mean-

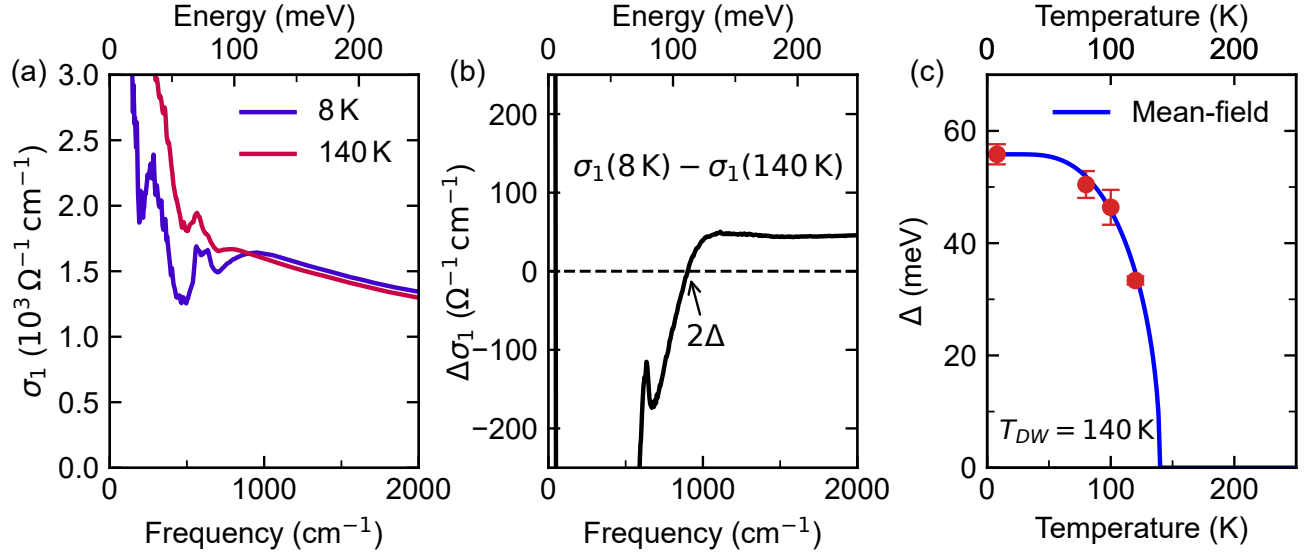


FIG. S4. Density wave energy gap and mean-field behavior. (a) and (b) display the in-plane optical conductivities and their difference at the lowest measured temperature 8 K, and just above the DW transition at 140 K. The opening of DW energy gap 2Δ is illustrated by the spectral weight transfer and crossing close to 1000 cm^{-1} . The evolution of energy gap Δ with temperature is shown in panel (c). The solid blue line denotes the mean-field behavior.

field curve by solving the self-consistent BCS gap equation and normalizing by the maximum gap and the DW transition temperature. To estimate uncertainties, we conservatively assume a relative reflectivity error of $\pm 0.5\%$ between temperatures, rescale $R(\omega)$ at all temperatures by factors of 1.005 and 0.995, recompute the corresponding conductivities, and re-extract Δ ; we take the difference between the gap values from the scaled reflectivities as the error bar, providing a conservative estimate of uncertainty from reflectivity errors. While the number of data points near T_{DW} is limited, the observed $\Delta(T)$ suggests that the DW transition is close to continuous and likely driven by an SDW instability, consistent with the Landau analysis of Ref.¹².

S4. ELECTRONIC CORRELATION CALCULATION

We quantify electronic correlations in $\text{La}_4\text{Ni}_3\text{O}_{10}$ using the ratio of experimental to band-theory kinetic energy, $K_{\text{exp}}/K_{\text{DFT}}$. To avoid contributions from interband transitions and phonons, we relate the kinetic energy to the Drude plasma frequency and compute $K_{\text{exp}}/K_{\text{DFT}} = \omega_{p,\text{exp}}^2/\omega_{p,\text{cal}}^2$. Because standard DFT does not capture DW effects, we use the experimental optical conductivity at 160 K (just above the DW transition) as the reference experimental spectrum. We perform the DFT calculation without including a Hubbard U . For the in-plane direction, a Drude+ ε_∞ fit to the measured $\sigma_{1,ab}(\omega)$ yields $\omega_{p,\text{exp}}^{ab} = 9855\text{ cm}^{-1}$ (1.222 eV), while DFT gives $\omega_{p,\text{cal}}^{ab} = 2.511\text{ eV}$, resulting in $K_{\text{exp}}^{ab}/K_{\text{DFT}}^{ab} = 0.237$, consistent with previous reports^{11,13}. For the out-of-plane direction, we obtain $\omega_{p,\text{exp}}^{c^*} = 402\text{ cm}^{-1}$ (0.050 eV) and $\omega_{p,\text{cal}}^{c^*} = 0.278\text{ eV}$, giving $K_{\text{exp}}^{c^*}/K_{\text{DFT}}^{c^*} = 0.032$.

Based on kinetic-energy ratios extracted from the optical plasma frequencies, $\text{La}_4\text{Ni}_3\text{O}_{10}$ is a moderately correlated metal in the in-plane direction, with $K_{\text{exp}}^{ab}/K_{\text{DFT}}^{ab} = 0.237$, while the out-of-plane response is strongly suppressed, yielding $K_{\text{exp}}^{c^*}/K_{\text{DFT}}^{c^*} = 0.032$. As summarized in Fig. S5, these values place $\text{La}_4\text{Ni}_3\text{O}_{10}$ in an intermediate regime relative to other layered nickelates and correlated oxides. The in-plane response is comparable to BaFe_2As_2 , where multiorbital physics is important, whereas the out-of-plane response resembles $\text{La}_3\text{Ni}_2\text{O}_7$ and La_2CuO_4 , which lie close to the Mott-insulating limit. This pronounced anisotropy reflects the layered crystal structure and the strongly reduced interlayer charge dynamics.

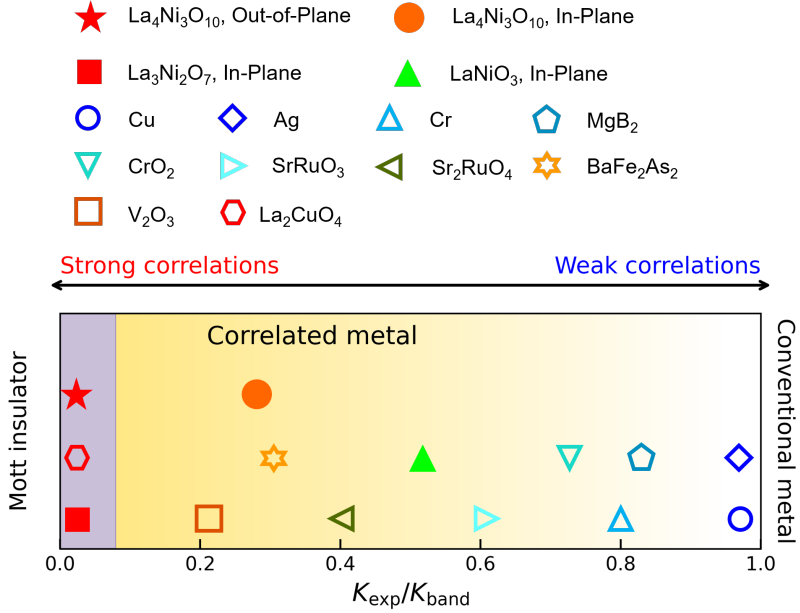


FIG. S5. Kinetic-energy ratio $K_{\text{exp}}/K_{\text{band}}$ for $\text{La}_4\text{Ni}_3\text{O}_{10}$ along the in-plane and out-of-plane directions, compared with the related nickelates $\text{La}_3\text{Ni}_2\text{O}_7$ and LaNiO_3 , and with other representative materials. For clarity, nickelates are shown as solid symbols and other materials as open symbols. $\text{La}_4\text{Ni}_3\text{O}_{10}$ is highlighted by a solid red star (out of plane) and a solid orange circle (in plane). Values of $K_{\text{exp}}/K_{\text{band}}$ are taken from Refs. ^{13–15} and references therein.

S5. DRUDE-LORENTZ FITTING

We use the multi-component Drude-Lorentz model to quantitatively analyze the temperature dependence of free carrier density, scattering rate, and phonon modes. The optical response of the material is modeled using a standard Drude-Lorentz formalism for the dimensionless complex dielectric function^{6,16},

$$\varepsilon(\omega) = \varepsilon_{\infty} - \sum_j \frac{\omega_{p,j}^2}{\omega^2 + i\gamma_j\omega} + \sum_k \frac{\omega_{p,k}^2}{\omega_{0,k}^2 - \omega^2 - i\gamma_k\omega}, \quad (\text{S1})$$

where the first summation describes the free-carrier response using one or more Drude terms, characterized by Drude plasma frequencies $\omega_{p,j}$ and Drude scattering rates γ_j . The second summation represents bound excitations modeled as Lorentz oscillators with resonance frequencies $\omega_{0,k}$, oscillator strengths $\omega_{p,k}$, and damping constants γ_k , which captures infrared-active phonons, interband transitions, and other finite energy excitations. The term ε_{∞} is the high-frequency dielectric constant accounting for polarization processes that occur at energies well above the spectral window explicitly modeled by the Drude and Lorentz terms. Physically, ε_{∞} incorporates mostly the cumulative contribution of core-electron and high-energy valence-electron screening that respond essentially instantaneously on the timescale of infrared excitations. As such, ε_{∞} provides a constant background that ensures the correct high-frequency limit of the dielectric function and should not be interpreted as the static dielectric constant.

The complex optical conductivity $\sigma(\omega)$ is directly related to the dielectric function via

$$\sigma(\omega) = \frac{\omega [\varepsilon(\omega) - 1]}{59.958 i}, \quad (\text{S2})$$

where the frequency ω is expressed in units of cm^{-1} and the resulting conductivity is obtained in units of $\Omega^{-1}\text{cm}^{-1}$. The numerical factor $59.958 \approx 60$ arises from unit conversion and corresponds to $Z_0/2\pi$, where Z_0 is the vacuum impedance^{6,16}. We use this formula to simultaneously fit the real and imaginary parts of the complex optical conductivity.

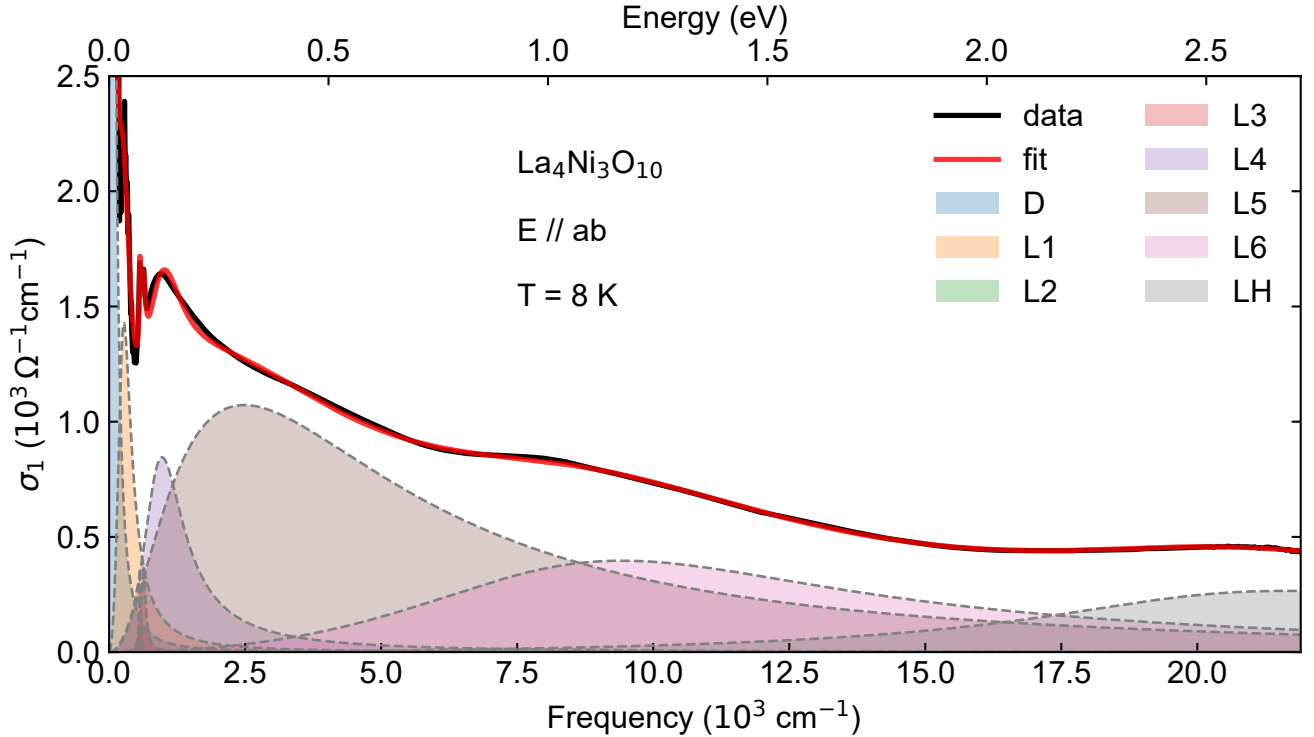


FIG. S6. The in-plane experimental $\sigma_1(\omega)$ (black curve) at 8 K and the Drude-Lorentz fitting result (red curve). Individual Drude and Lorentz components are shown as shaded areas.

Fig. S6 shows the Drude-Lorentz fit to the in-plane optical conductivity at 8 K. We model multiple interband transitions with a set of Lorentz oscillators and include a phonon-like feature near 600 cm^{-1} . The fitted interband structure broadly follows DFT, although the oscillator strengths differ quantitatively, and fewer distinct modes are resolved experimentally, consistent with substantial spectral broadening.

In RP nickelates, the low-frequency response is sometimes parameterized with multiple Drude components to reflect multiband character and possible orbital-dependent scattering^{11,15}. When these intraband contributions are not spectroscopically resolved, however, such decompositions are not unique and increase correlations among parameters. Here, the low-frequency conductivity is a single, smooth Drude-like component, without clear signatures that uniquely require multiple Drude terms. Hence, we adopt a minimal intraband description to capture the essential charge dynamics while limiting model dependence.

We also compare two fitting strategies for the in-plane response in Fig. S7: (i) a full-range Drude-Lorentz fit over the entire measured window and (ii) a simple single Drude+ ε_∞ fit. The extracted plasma frequency, scattering rate, and DC resistivity from the two approaches agree within uncertainties, supporting the Drude+ ε_∞ analysis used in the main text as a reliable description of the in-plane free-carrier response.

For the out-of-plane response, the Drude spectral weight is much smaller, so full-range Drude-Lorentz fits become dominated by higher-frequency contributions. The resulting low-energy Drude parameters depend sensitively on the high-frequency modeling and are therefore not robust. We thus avoid full-range Drude-Lorentz fits for the *c*-axis data and instead rely on a low-frequency Drude+ ε_∞ analysis.

We observe that the in-plane response the squared Drude plasma frequency ω_p^2 , which is proportional to the effective free-carrier density, is reduced by approximately 25% upon cooling from high temperature to low temperature. This suppression indicates a partial depletion of the in-plane Fermi surface, consistent with the opening of a density-wave-induced gap that removes a fraction of the itinerant carriers¹¹.

Fig. S8 shows the Drude-Lorentz fit to the out-of-plane optical conductivity at 4 K. We model high-energy interband

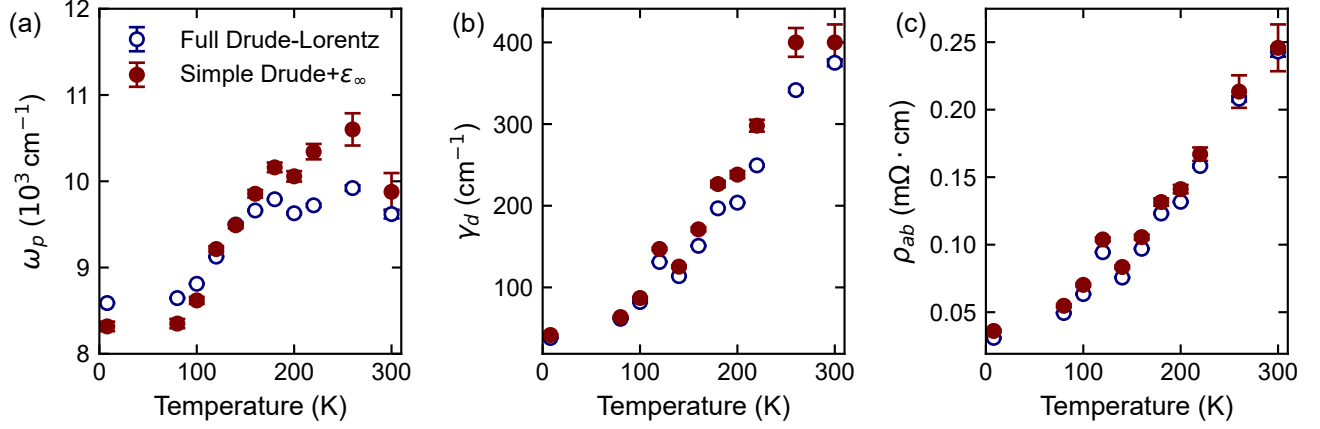


FIG. S7. Comparison of (a) in-plane Drude plasma frequency ω_p , (b) scattering rate γ_d , and (c) DC resistivity ρ_{ab} obtained from full-range Drude-Lorentz fitting (blue open circles) and low-frequency Drude+ ε_∞ analysis (red filled circles) and as function of temperature.

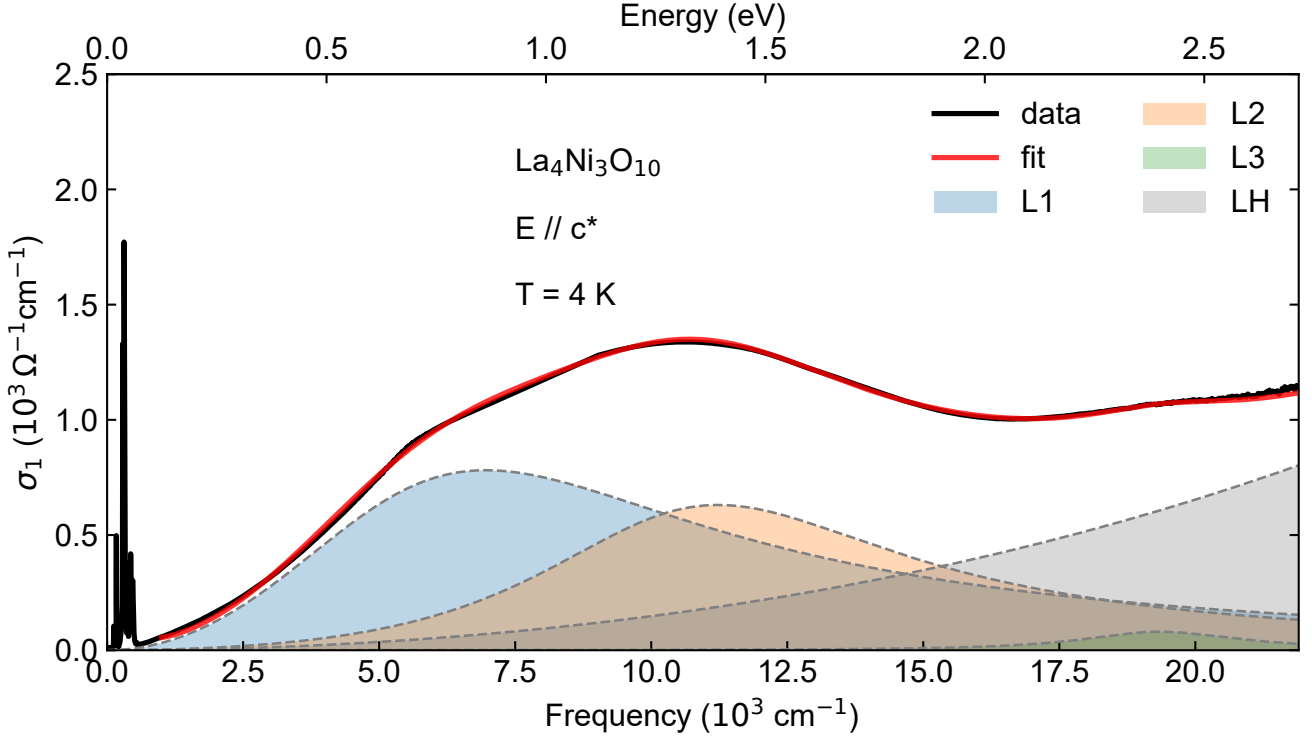


FIG. S8. Out-of-plane experimental $\sigma_1(\omega)$ (black curve) at 4 K and the Drude-Lorentz fit (red curve). Individual Lorentz components are shown as shaded areas.

transitions ($> 1000 \text{ cm}^{-1}$) with a set of Lorentz oscillators, while we defer the detailed Drude-Lorentz analysis of phonons below 600 cm^{-1} to Sec. S7. As for the in-plane response, the fitted interband structure broadly agrees with DFT, although the oscillator strengths differ quantitatively and fewer modes are resolved experimentally, consistent with substantial spectral broadening.

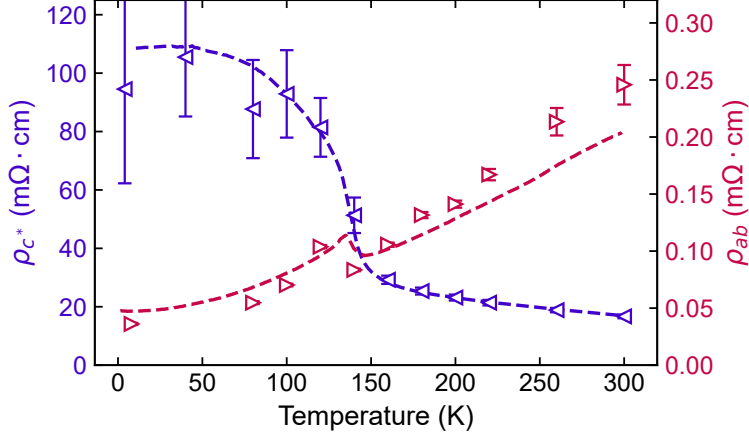


FIG. S9. Comparison between DC resistivity extracted from optical (triangles with error bars) and transport measurements (broken lines) on $\text{La}_4\text{Ni}_3\text{O}_{10}$ along both in-plane and out-of-plane directions. The in-plane transport resistivity ρ_{ab} data are adapted and rescaled from Ref.¹.

S6. TRANSPORT RESISTIVITY

To further validate the temperature-dependent anisotropy extracted from the optical conductivity, we compare the DC resistivity inferred from optics with transport measurements. Transport resistivity carries inherent systematic uncertainties, most notably geometric factors used to convert resistance to resistivity, and overall uncertainties can approach an order of magnitude. A major advantage of optical spectroscopy is to provide low-frequency limit resistivity free from the geometric uncertainties. For this reason, in comparing to transport we apply an overall rescaling factor to the transport data to account for its absolute uncertainty.

For the in-plane resistivity, we use published transport data from Ref.¹, shown as the cardinal red dashed line in Fig. S9 after applying a uniform rescaling factor of 0.15. Since no out-of-plane resistivity has been reported for $\text{La}_4\text{Ni}_3\text{O}_{10}$, we measured ρ_{c^*} using a standard four-probe technique on a polished ac^* -plane sample, varying temperature from 10 K to 300 K in a He^4 gas-flow cryostat. The measured out-of-plane $\rho_{c^*}(T)$ is also rescaled by a constant factor for plotting in Fig. S9, to align with the optically extrapolated DC resistivity. We note that in highly anisotropic systems such as $\text{La}_4\text{Ni}_3\text{O}_{10}$ it is difficult to eliminate mixing of in- and out-of-plane channels in a conventional four-probe geometry, and some sample-to-sample dispersion is also expected^{1,17,18}. With these caveats in mind, the temperature dependence of our measured $\rho_{c^*}(T)$ closely resembles the reported out-of-plane resistivity trend of $\text{Pr}_4\text{Ni}_3\text{O}_{10}$ in Ref.¹⁹. Overall, the in-plane and out-of-plane resistivities inferred from the optical Drude analysis are in reasonable agreement with the transport data at the level of temperature trends. We emphasize that, due to experimental schematics and sample-to-sample dispersion, the absolute value of ρ_{c^*}/ρ_{ab} should be taken as an estimate, while the temperature trend is the more robust result.

S7. PHONON MODES: FITTING

We fit the c^* -axis optical conductivity with a Drude-Lorentz model over the full temperature range, restricting the window to $\omega < 600 \text{ cm}^{-1}$ to include all observed infrared-active phonons while excluding higher-energy interband transitions. Fits at 4 K (Fig. S10) and 160 K (Fig. S11) are shown as representative examples well below and above the DW transition, respectively. In both cases, simultaneous fits to the real and imaginary parts of the complex conductivity capture the main features, enabling a systematic analysis of the phonon evolution with temperature.

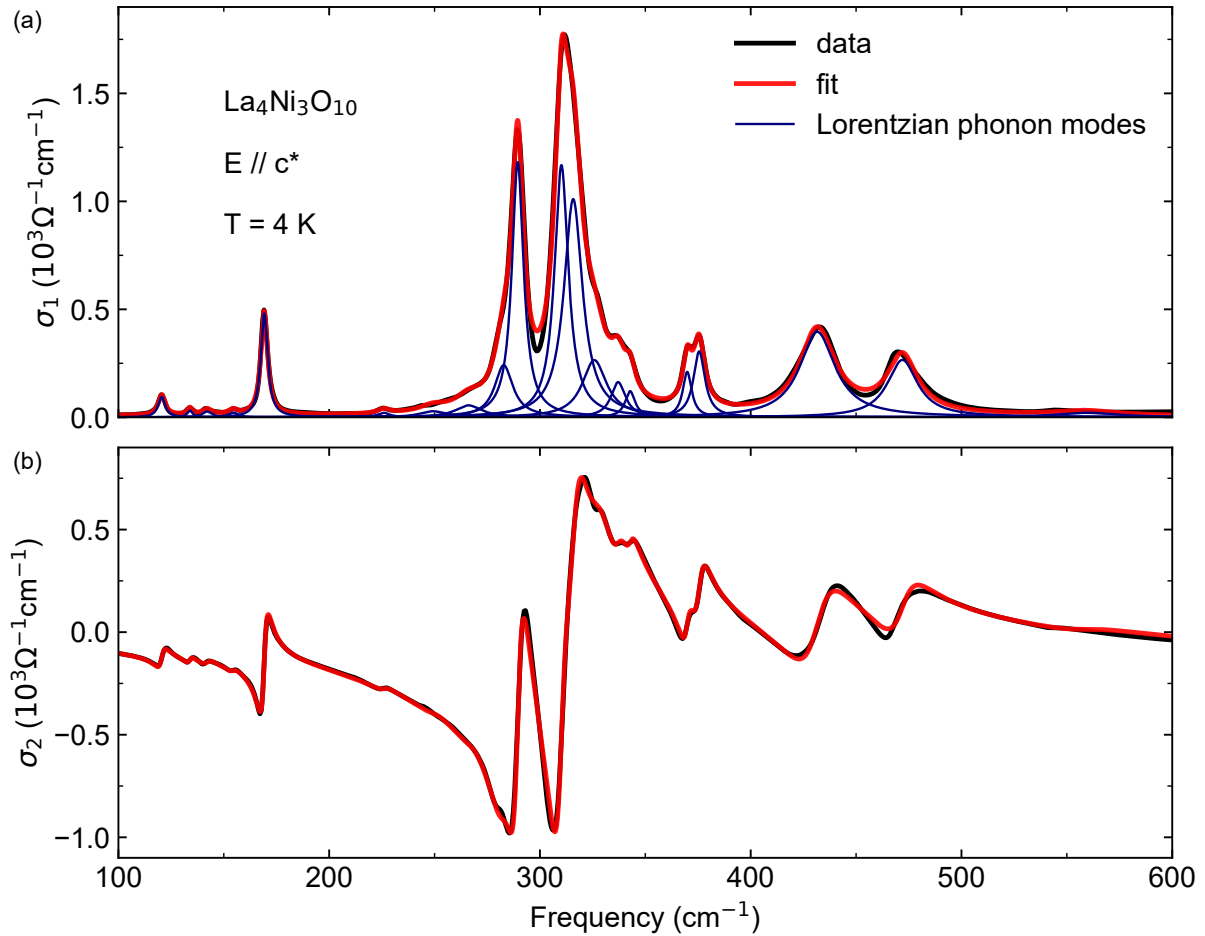


FIG. S10. Real and imaginary optical conductivity $\sigma_1(\omega)$ and $\sigma_2(\omega)$ at 4 K in the range of $100\text{--}600\text{ cm}^{-1}$. The solid red line is the Drude-Lorentz fit of the experimental data (black solid line). Thin navy solid lines correspond to individual Lorentzian phonon modes. We identify a total of 20 modes at 4 K.

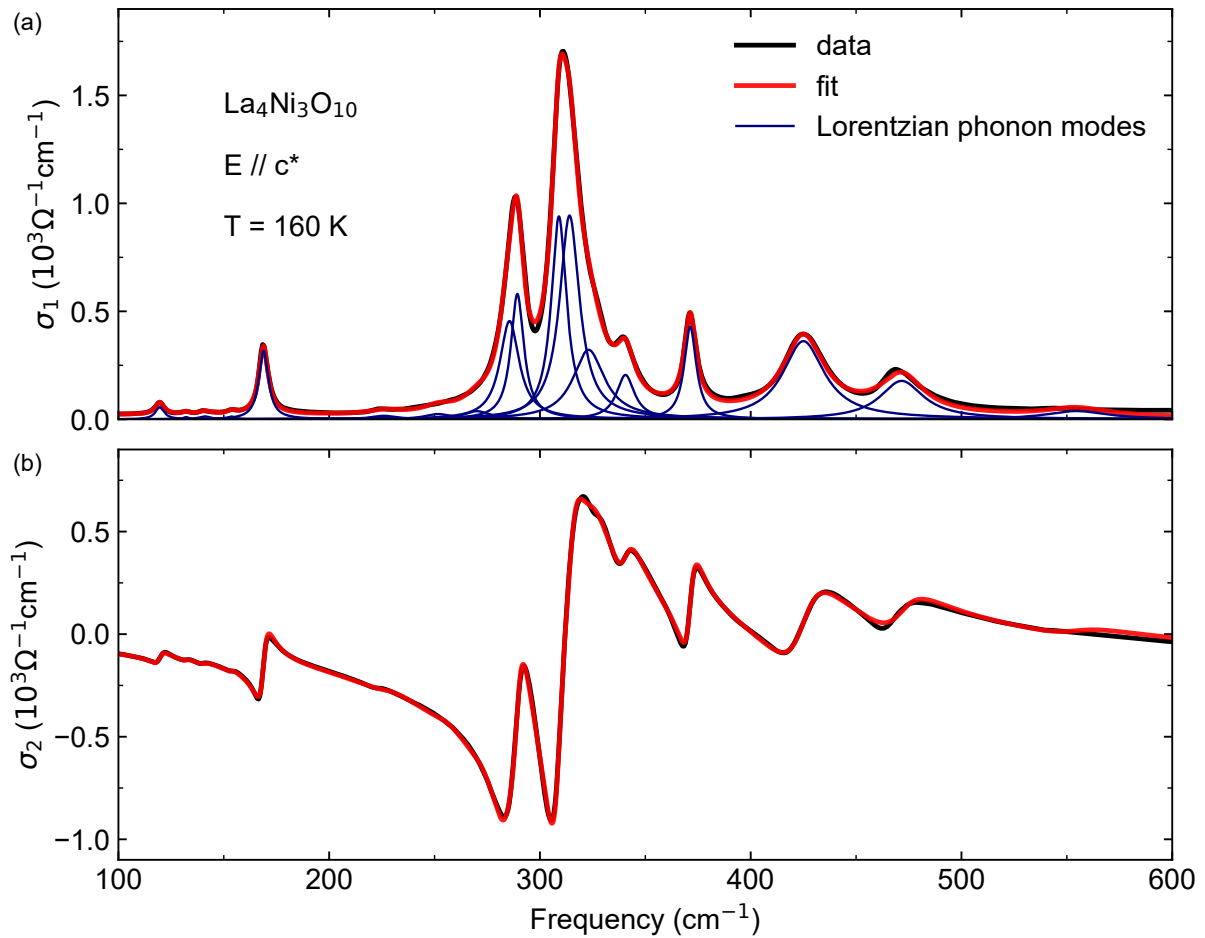


FIG. S11. Real and imaginary optical conductivity $\sigma_1(\omega)$ and $\sigma_2(\omega)$ at 160 K in the range of 100-600 cm^{-1} . The solid red line is the Drude-Lorentz fit of the experimental data (black solid line). Thin navy solid lines correspond to individual Lorentzian phonon modes. We identify total of 18 modes at 160 K.

S8. PHONON MODES: COMPARISON WITH DFT

At ambient-pressure, $\text{La}_4\text{Ni}_3\text{O}_{10}$ crystallizes in the monoclinic $P2_1/a$ structure and the structural symmetry is preserved across the DW transition^{17,18,20}. This structure with two formula units per primitive unit cell ($Z = 2$) supports a total of 102 normal modes at the Brillouin zone center: 3 acoustic and 99 optical modes. These modes decompose into $24A_g + 26A_u + 24B_g + 25B_u$ representations, where the odd-parity A_u and B_u modes are infrared-active and the even-parity A_g and B_g modes are Raman-active. In the conventional monoclinic $P2_1/a$ setting (unique b axis), the infrared-active modes decompose into A_u modes with dipole moments primarily along b , and B_u modes with dipole in the ac plane. Thus, an out-of-plane polarized experiment is expected to predominantly probe B_u modes. The monoclinic tilt angle ($\beta \approx 100.8^\circ$, i.e. $\sim 11^\circ$ between the crystallographic c direction and the experimental out-of-plane c^* direction¹) together with crystal twinning effects and a small (possible) miscut can mix components, so both A_u and B_u modes may acquire finite intensity for the out-of-plane measurement.

Given the large number of symmetry-allowed optical modes and the monoclinic symmetry, we use first-principles calculations to guide the identification of corresponding modes. We perform phonon calculations within density functional theory using the finite-displacement method. We carry out the electronic-structure calculations with the Vienna *ab initio* Simulation Package (VASP) using the GGA-PBE exchange-correlation functional⁸. We base the calculations on the experimentally determined monoclinic $P2_1/a$ structure of $\text{La}_4\text{Ni}_3\text{O}_{10}$, with structural data taken from Ref. ¹. We obtain interatomic force constants with PHONOPY²¹ by finite displacements in a $2 \times 2 \times 1$ supercell, corresponding to a doubling of the in-plane unit cell. We then use these force constants to compute zone-center phonon frequencies and eigenvectors.

Table S1 compares the DFT zone-center frequencies of infrared-active phonons with the mode frequencies extracted from Drude-Lorentz fits at 160 K and 4 K. At 160 K, above the density-wave transition, we associate the fitted out-of-plane modes with nearby calculated infrared-active modes based on frequency proximity and the calculated oscillator strengths of the out-of-plane dipole component. By contrast, at 4 K (below T_{DW}) we resolve additional phonon modes that have no direct counterparts among the calculated modes.

TABLE S1. Comparison of extracted phonon modes from Drude-Lorentz fits at 160 K and 4 K to calculated infrared-active phonon modes. The DFT mode labels ($P\#$) follow the ranking of the phonon frequencies among all 102 calculated modes.

DFT modes	DFT (cm^{-1})	160 K fit (cm^{-1})	4 K fit (cm^{-1})
$P18$	120.6	119.6 ± 0.1	120.5 ± 0.1
$P20$	125.5	132.0 ± 0.3	133.9 ± 0.2
$P23$	137.3	140.9 ± 0.4	142.0 ± 0.3
$P26$	144.2	153.5 ± 0.3	154.4 ± 0.3
$P28$	152.1	$168.8 \pm < 0.1$	$169.2 \pm < 0.1$
$P46$	227.5	225.9 ± 0.8	225.9 ± 0.6
$P48$	234.0	251.6 ± 0.7	249.2 ± 1.1
$P54$	268.3	270.0 ± 0.7	266.1 ± 0.6
$P57$	286.2	285.6 ± 0.4	282.8 ± 0.2
$P60$	296.0	289.3 ± 0.1	$289.5 \pm < 0.1$
$P62$	303.8	309.0 ± 0.1	310.2 ± 0.1
$P64$	307.6	314.0 ± 0.2	315.8 ± 0.1
$P68$	316.4	323.1 ± 0.6	325.8 ± 0.4
$P76$	353.3	340.6 ± 0.1	337.1 ± 0.3 342.8 ± 0.3
$P81$	390.9	$371.3 \pm < 0.1$	369.9 ± 0.1 375.6 ± 0.1
$P86$	434.4	425.0 ± 0.1	431.6 ± 0.1
$P93$	501.1	471.6 ± 0.2	472.0 ± 0.2
$P100$	573.9	554.5 ± 1.2	558.9 ± 3.6

S9. PHONON MODES: ANOMALY AND ATOMIC DISPLACEMENT

Across the DW transition, reported lattice-parameter anomalies are well below the level of 0.1% in relative magnitude^{1,17,18,20}. A simple way to estimate the size of phonon shifts expected from such small structural changes is via a mode Grüneisen parameter γ_i , defined by

$$\frac{\Delta\omega_i}{\omega_i} \approx -\gamma_i \frac{\Delta V}{V}, \quad (S3)$$

(or an anisotropic analog using linear strains). The Grüneisen parameter, γ_i , is usually of order unity for common solid-state materials, even taking a conservative upper bound $\gamma_i \sim 2\text{-}3$ ^{22,23}, lattice/volume changes below 0.1% level would imply $\Delta\omega/\omega \lesssim 0.1\text{-}0.3\%$. This estimate is well below the $\sim 1\%$ frequency anomalies and splittings we observe, and, importantly, such anomalies are highly mode-selective (confined to the 300-500 cm⁻¹ window) rather than a broadly distributed hardening/softening expected from uniform strain. This comparison supports that the dominant phonon renormalization is tied to the DW electron-phonon/magnetoelastic coupling rather than a simply structural anomaly.

To quantify the temperature dependence of the phonon anomalies, we analyze the evolution of phonon frequency $\omega_0(T)$ and scattering rate (linewidth) $\gamma(T)$ extracted from the Drude-Lorentz fits. The high-temperature behavior is described by the Klemens-Hart-Agarwal-Lax model²⁴. In this model, cubic anharmonic decay of phonons gives the temperature dependence of the phonon frequency and the scattering rate as

$$\begin{aligned} \omega_0(T) &= \omega_{0,T=0} + A \cdot \left(1 + \frac{2}{e^x - 1} \right), \\ \gamma(T) &= \gamma_{\text{res}} + B \cdot \left(1 + \frac{2}{e^x - 1} \right), \end{aligned} \quad (S4)$$

with $x = \frac{\hbar\omega_{0,T=0}}{2k_B T}$.

Here, $\omega_{0,T=0}$ denotes the bare phonon frequency at zero temperature, γ_{res} represents a temperature-independent residual scattering rate that captures additional broadening mechanisms not accounted for by anharmonic decay, and A, B are constants. Fits using these expressions are restricted to the high-temperature regime, and deviations from the extrapolated behavior at low temperatures reflect strong phonon renormalization induced by the DW transition.

The phonon anomalies induced by the DW transition are found primarily in the frequency range between 300 and 500 cm⁻¹. We therefore focus on four phonon modes in this window that exhibit the most pronounced deviations from conventional anharmonic behavior. Two modes, located near 371 cm⁻¹ (Fig. S12) and 340 cm⁻¹ (Fig. S13) in the high-temperature phase, split into distinct branches upon cooling to the DW state. In addition, two higher-frequency modes near 430 cm⁻¹ (Fig. S14) and 475 cm⁻¹ (Fig. S15) show strong renormalization without a resolvable splitting. For all four modes, the temperature dependence of the resonance frequency and linewidth is analyzed using the anharmonic decay model described above. By contrast, phonon modes outside this frequency window, such as the mode near 169 cm⁻¹ shown in Fig. S18, exhibit temperature evolutions that remain well described by conventional anharmonic behavior over the full temperature range. This comparison highlights the non-uniform and energy-selective nature of the DW-phonon coupling, with the strongest deviations from anharmonicity occurring for modes in the frequency range between approximately 370 and 430 cm⁻¹. Notably, this range coincides with the typical energy scale of Ni-O bond-stretching vibrations, suggesting that lattice distortions involving Ni-O bond are particularly sensitive to the electronic modulation associated with the DW transition. To further elucidate the lattice degrees of freedom underlying the phonon anomalies, we examine the calculated displacement patterns of the four representative modes discussed above. As shown in Fig. S16, these modes are dominated by Ni-O bond bending, suggesting that Ni-O distortions are especially sensitive to the electronic reconstruction across the DW transition. Consistent with this interpretation, additional DFT calculated eigenvectors for other modes in the same 300-500 cm⁻¹ window also exhibit substantial participation of the Ni-O bonds, even though these modes are not associated to experimentally observed phonons (Fig. S17).

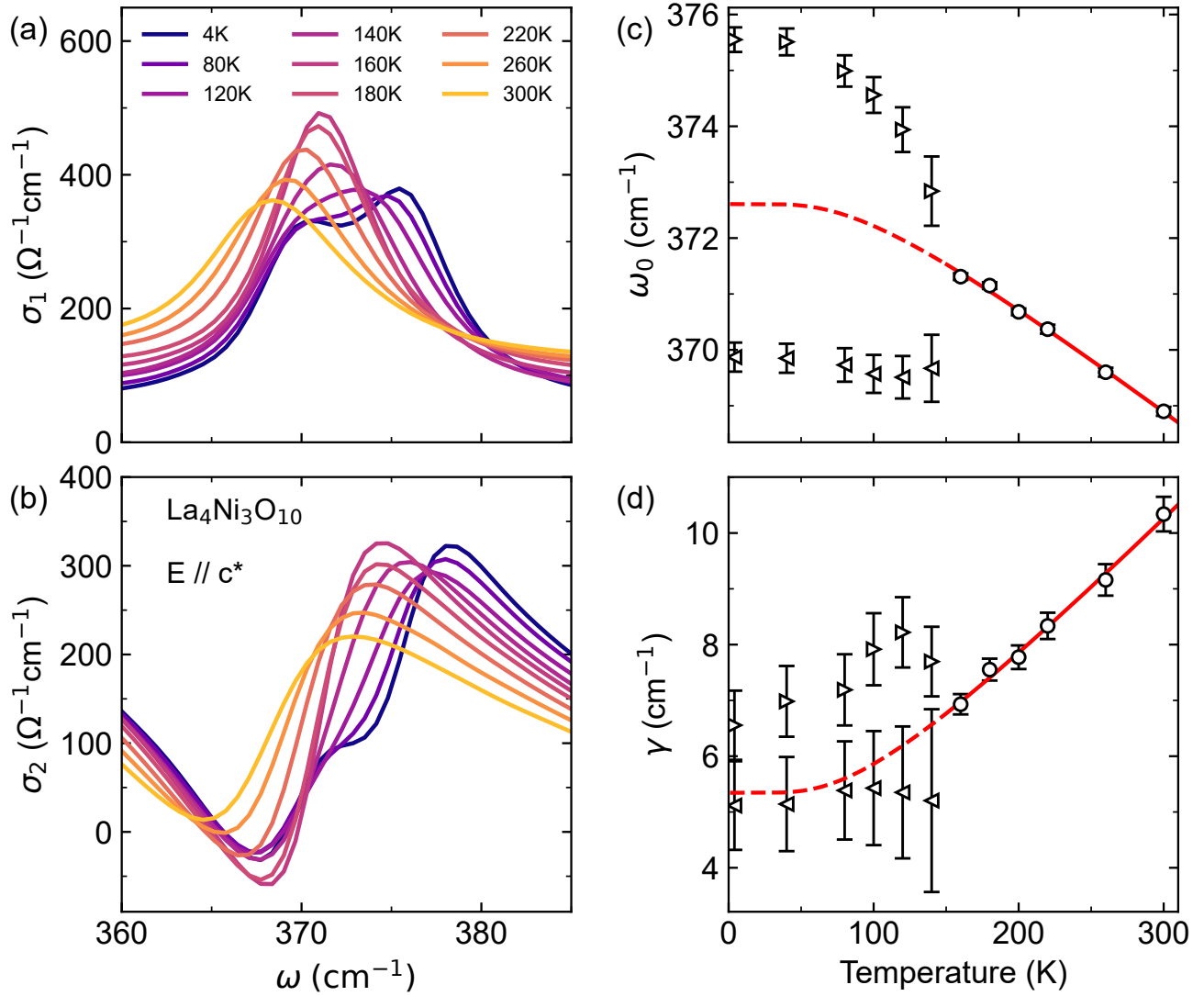


FIG. S12. (a), (b) Real and imaginary out-of-plane optical conductivity of $\text{La}_4\text{Ni}_3\text{O}_{10}$ in a narrow frequency window around the 371 cm^{-1} mode. (c), (d) Temperature dependence of the fitted phonon frequency ω_0 and scattering rate γ for the modes near near 371 cm^{-1} . On cooling below the density-wave (DW) transition, this phonon splits into two distinct low-temperature branches that evolve from a single high-temperature mode. Solid red curves show anharmonic phonon-decay fits to the high-temperature data, and dashed curves extrapolate the fits to low temperature. The strong deviation of the measured low-temperature phonon parameters from the extrapolated anharmonic trend indicates substantial DW-associated phonon renormalization.

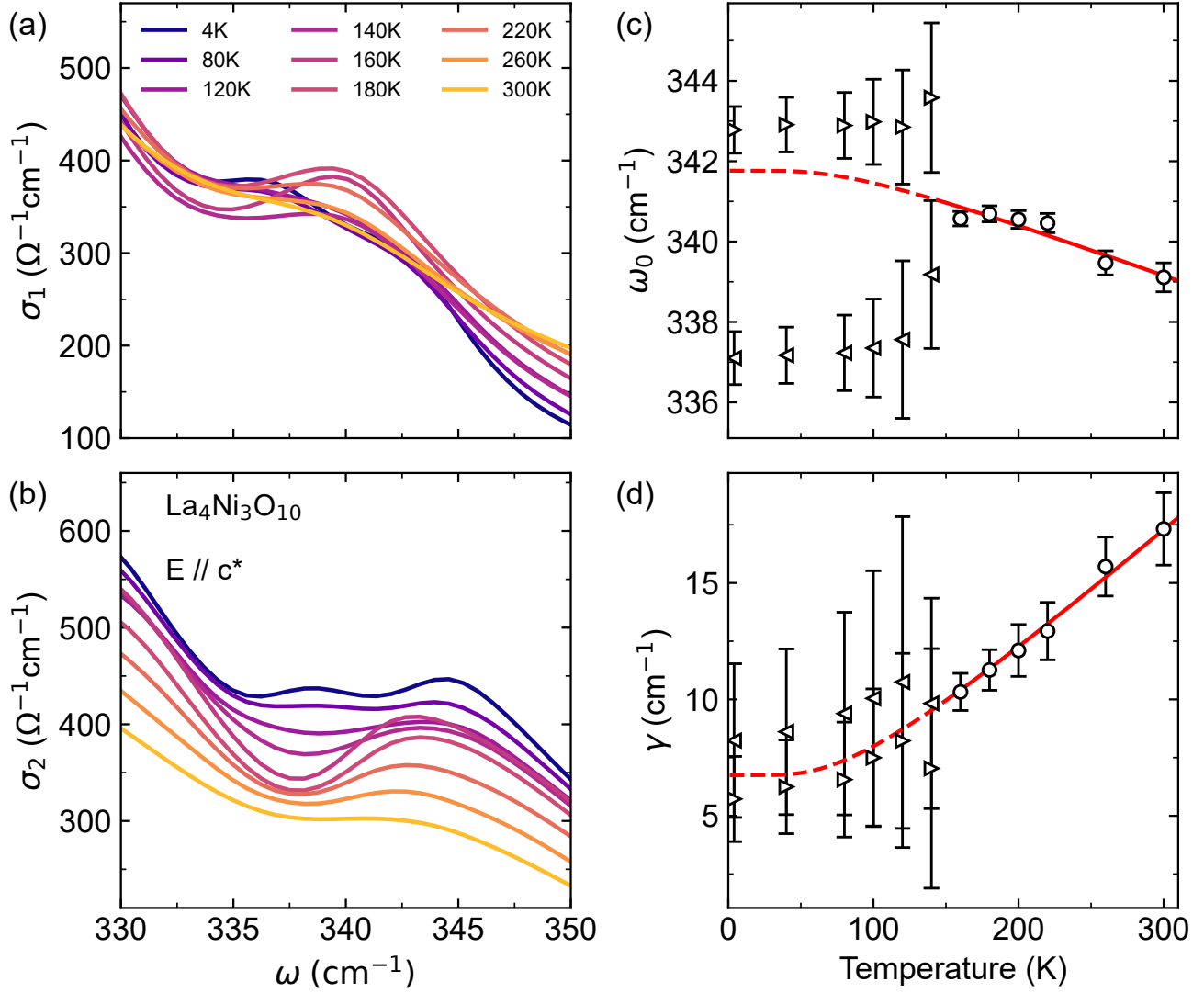


FIG. S13. (a), (b) Real and imaginary out-of-plane optical conductivity of $\text{La}_4\text{Ni}_3\text{O}_{10}$ in a narrow frequency window around the 340 cm^{-1} mode. (c), (d) Temperature dependence of the fitted phonon frequency ω_0 and scattering rate γ for the modes near 340 cm^{-1} . The phonon mode exhibits a subtle splitting below the DW transition, most clearly resolved in the imaginary part of the optical conductivity $\sigma_2(\omega)$. Solid red curves represent fits to the high-temperature data using an anharmonic phonon decay model, whereas dashed lines indicate extrapolations into the low-temperature regime. The deviation between the low-temperature phonon parameters and the extrapolated anharmonic behavior reflects a DW-induced phonon renormalization.

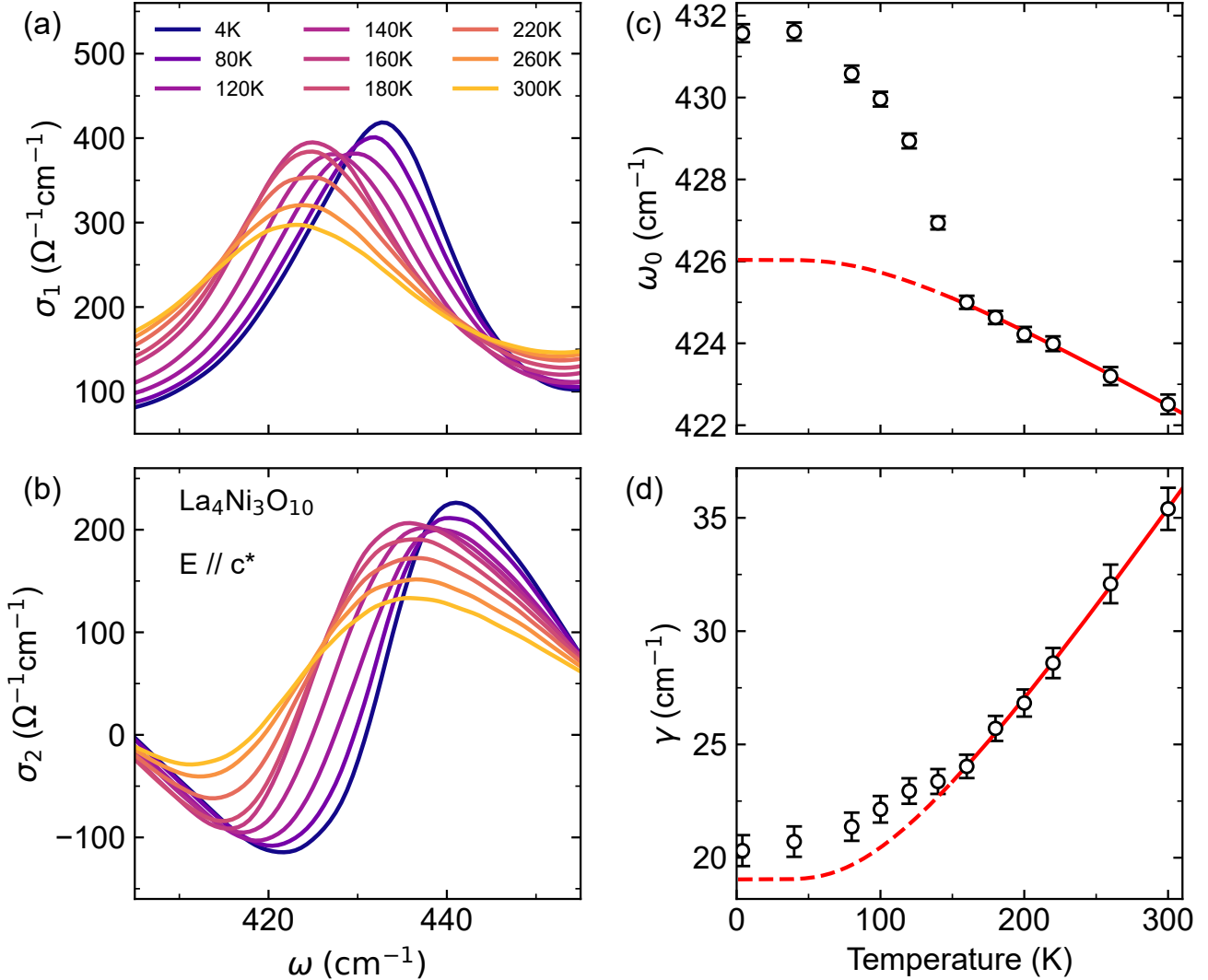


FIG. S14. (a), (b) Real and imaginary out-of-plane optical conductivity of $\text{La}_4\text{Ni}_3\text{O}_{10}$ in a narrow frequency window around the 430 cm^{-1} mode. (c), (d) Temperature dependence of the fitted phonon frequency ω_0 and scattering rate γ for the modes near 430 cm^{-1} . Unlike the lower-energy modes, this phonon shows no resolvable splitting, but its frequency and linewidth renormalize strongly on cooling below the DW transition. Solid red curves show anharmonic phonon-decay fits to the high-temperature data, and dashed curves extrapolate the fits to low temperature. The marked deviation of the low-temperature phonon parameters from the extrapolated anharmonic trend signals strong DW-induced renormalization.

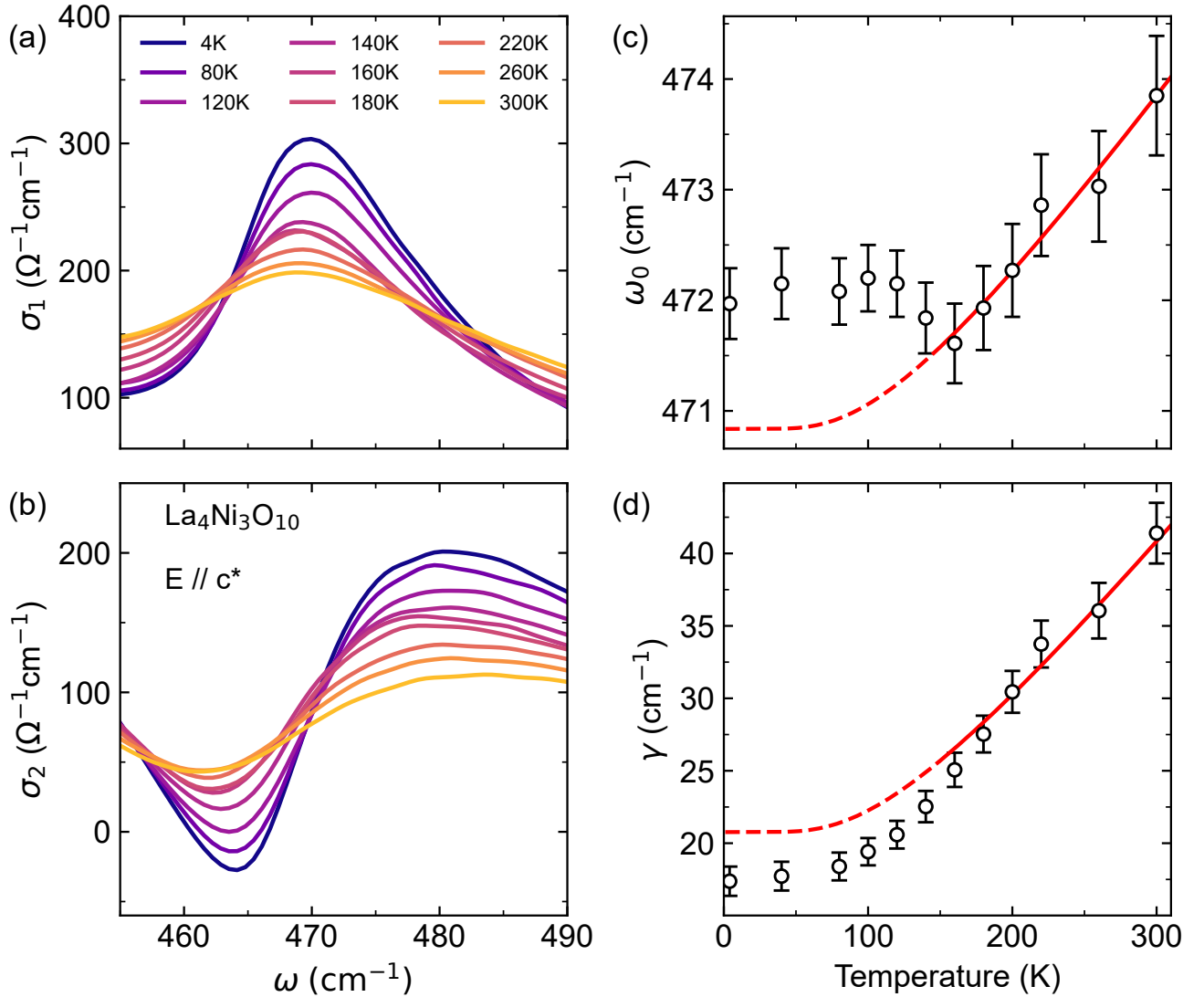


FIG. S15. (a), (b) Real and imaginary out-of-plane optical conductivity of $\text{La}_4\text{Ni}_3\text{O}_{10}$ in a narrow frequency window around the 475 cm^{-1} mode. (c), (d) Temperature dependence of the fitted phonon frequency ω_0 and scattering rate γ for the modes near 475 cm^{-1} . As for the mode near 430 cm^{-1} , this phonon shows no clear splitting but undergoes a strong renormalization of its frequency and linewidth below the DW transition. Solid red curves show anharmonic phonon-decay fits to the high-temperature data, and dashed curves extrapolate the fits to low temperature. The deviation of the measured low-temperature parameters from the extrapolated anharmonic trend further highlights the strong impact of the DW transition on the lattice dynamics.

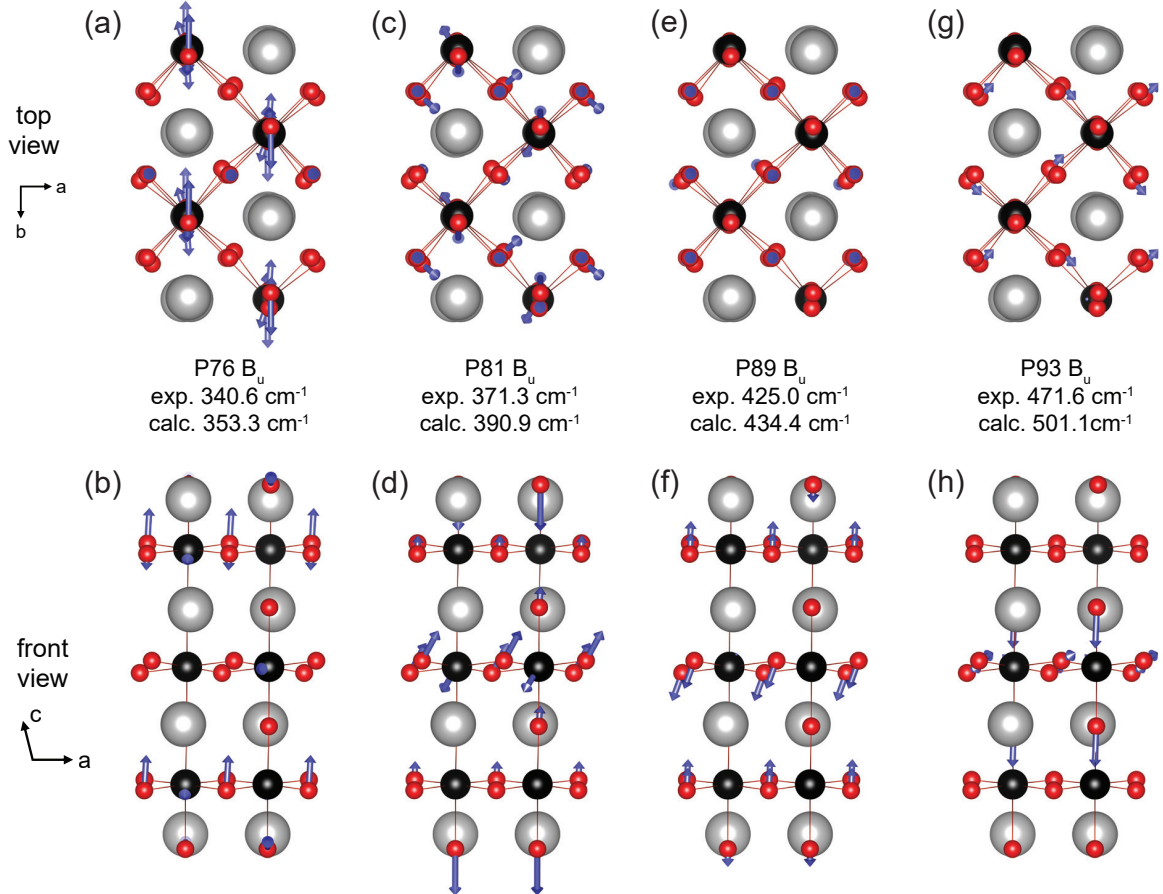


FIG. S16. Calculated atomic displacement patterns for four representative infrared-active phonon modes that exhibit pronounced anomalies across the density-wave transition. Panels (a,b), (c,d), (e,f), and (g,h) show the top and front views of the phonon eigenvectors for modes near 340 cm^{-1} (P76), 371 cm^{-1} (P81), 430 cm^{-1} (P86), and 475 cm^{-1} (P93), respectively. The corresponding experimental (at 160 K) and calculated phonon frequencies are indicated for each mode. The mode labels (P#) follow the ranking of the phonon frequencies among all 102 calculated zone-center phonon modes, consistent with the notation used in Table S1. For clarity, only displacements with large amplitude are shown for each mode.

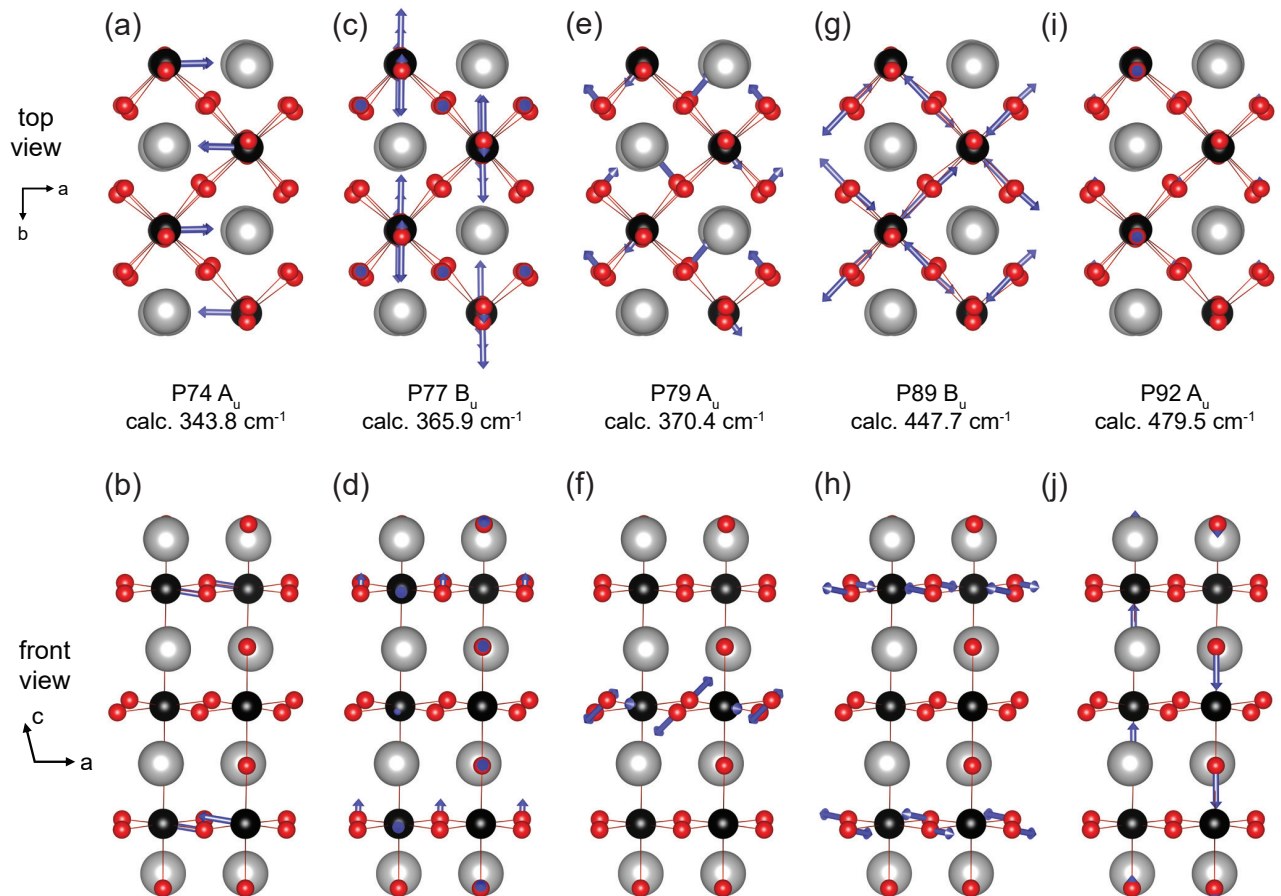


FIG. S17. Calculated atomic displacement patterns for other infrared-active phonon modes in the frequency range between 300 and 500 cm^{-1} . Panels (a,b), (c,d), (e,f), (g,h), and (i,j) show the top and front views of the phonon eigenvectors for modes P74, P77, P79, P89, and P92, respectively. The corresponding calculated phonon frequencies are indicated for each mode. The mode labels (P#) follow the ranking of the phonon frequencies among all 102 calculated zone-center phonon modes. For clarity, only displacements with large amplitude are shown for each mode. These representative eigenvectors illustrate that phonons in this frequency window primarily involve vibrations of the Ni-O bonds (including Ni-O stretching and bending character), consistent with the discussion in the main text.

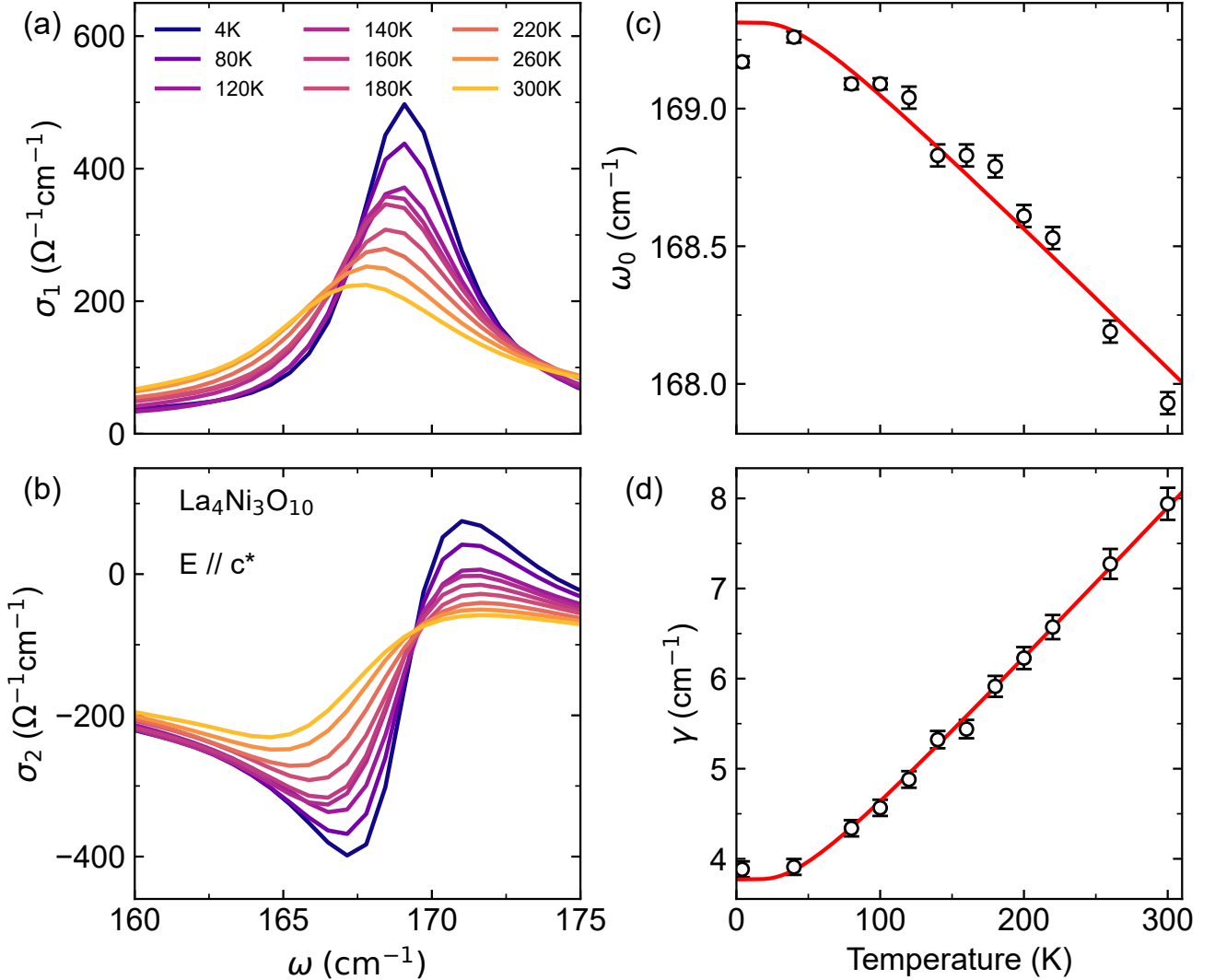


FIG. S18. (a), (b) Real and imaginary out-of-plane optical conductivity of $\text{La}_4\text{Ni}_3\text{O}_{10}$, in a narrow frequency window around the 169 cm^{-1} mode. (c), (d) Temperature dependence of the fitted phonon frequency ω_0 and scattering rate γ for the modes. In contrast to the pronounced anomalies of selected modes between 300 and 500 cm^{-1} , the phonon near 169 cm^{-1} shows no discernible renormalization of its frequency or linewidth across the DW transition. Solid red curves show anharmonic phonon-decay fits over the full temperature range. The good agreement indicates that this mode is largely insensitive to the DW transition, underscoring the mode and energy selectivity of DW-induced phonon modulation.

¹ Junjie Zhang, Hong Zheng, Yu-Sheng Chen, Yang Ren, Masao Yonemura, Ashfia Huq, and J. F. Mitchell, “High oxygen pressure floating zone growth and crystal structure of the metallic nickelates $R_4Ni_3O_{10}$ (R = La, Pr),” *Phys. Rev. Mater.* **4**, 083402 (2020).

² Christopher C. Homes, M. Reedyk, D. A. Cradles, and T. Timusk, “Technique for measuring the reflectance of irregular, submillimeter-sized samples,” *Appl. Opt.* **32**, 2976–2983 (1993).

³ C. C. Homes, J. M. Tranquada, and D. J. Buttrey, “Stripe order and vibrational properties of $La_2NiO_{4+\delta}$ for $\delta = 2/15$: measurements and *ab initio* calculations,” *Phys. Rev. B* **75**, 045128 (2007).

⁴ Hari Padma, Filippo Glerean, Sophia F. R. TenHuisen, Zecheng Shen, Haoxin Wang, Luogen Xu, Joshua D. Elliott, Christopher C. Homes, Elizabeth Skoropata, Hiroki Ueda, Biaolong Liu, Eugenio Paris, Arnau Romaguera, Byungjune Lee, Wei He, Yu Wang, Seng Huat Lee, Hyeongi Choi, Sang-Youn Park, Zhiqiang Mao, Matteo Calandra, Hoyoung Jang, Elia Razzoli, Mark P. M. Dean, Yao Wang, and Matteo Mitrano, “Symmetry-protected electronic metastability in an optically driven cuprate ladder,” *Nat. Mater.* **24**, 1584–1591 (2025), issue date: Oct 2025.

⁵ Frank Y. Gao, Zhuquan Zhang, Zi-Jie Liu, and Keith A. Nelson, “High-speed two-dimensional terahertz spectroscopy with echelon-based shot-to-shot balanced detection,” *Opt. Lett.* **47**, 3479–3482 (2022).

⁶ D. B. Tanner, “Use of x-ray scattering functions in Kramers-Kronig analysis of reflectance,” *Phys. Rev. B* **91**, 035123 (2015).

⁷ Peter Blaha, Karlheinz Schwarz, Fabien Tran, Robert Laskowski, Georg K. H. Madsen, and Laurence D. Marks, “WIEN2k: An APW+lo program for calculating the properties of solids,” *J. Chem. Phys.* **152**, 074101 (2020).

⁸ John P. Perdew, Kieron Burke, and Matthias Ernzerhof, “Generalized gradient approximation made simple,” *Phys. Rev. Lett.* **77**, 3865–3868 (1996).

⁹ A. Seidl, A. Görling, P. Vogl, J. A. Majewski, and M. Levy, “Generalized Kohn-Sham schemes and the band-gap problem,” *Phys. Rev. B* **53**, 3764–3774 (1996).

¹⁰ Haoxiang Li, Xiaoqing Zhou, Thomas Nummy, Junjie Zhang, Victor Pardo, Warren E. Pickett, J. F. Mitchell, and D. S. Dessau, “Fermiology and electron dynamics of trilayer nickelate $La_4Ni_3O_{10}$,” *Nat. Commun.* **8**, 704 (2017).

¹¹ Shuxiang Xu, Cui-Qun Chen, Mengwu Huo, Deyuan Hu, Hao Wang, Qiong Wu, Rongsheng Li, Dong Wu, Meng Wang, Dao-Xin Yao, Tao Dong, and Nanlin Wang, “Origin of the density wave instability in trilayer nickelate $La_4Ni_3O_{10}$ revealed by optical and ultrafast spectroscopy,” *Phys. Rev. B* **111**, 075140 (2025).

¹² M. R. Norman, “Landau theory of the density wave transition in trilayer Ruddlesden-Popper nickelates,” *Phys. Rev. B* **112**, 075149 (2025).

¹³ Zhe Liu, Jie Li, Mengwu Huo, Bingke Ji, Jiahao Hao, Yaomin Dai, Mengjun Ou, Qing Li, Hualei Sun, Bing Xu, Yi Lu, Meng Wang, and Hai-Hu Wen, “Evolution of electronic correlations in the Ruddlesden-Popper nickelates,” *Phys. Rev. B* **111**, L220505 (2025).

¹⁴ M. M. Qazilbash, J. J. Hamlin, R. E. Baumbach, Lijun Zhang, D. J. Singh, M. B. Maple, and D. N. Basov, “Electronic correlations in the iron pnictides,” *Nat. Phys.* **5**, 647–650 (2009).

¹⁵ Zhe Liu, Mengwu Huo, Jie Li, Qing Li, Yuecong Liu, Yaomin Dai, Xiaoxiang Zhou, Jiahao Hao, Yi Lu, Meng Wang, and Hai-Hu Wen, “Electronic correlations and partial gap in the bilayer nickelate $La_3Ni_2O_7$,” *Nat. Commun.* **15**, 7570 (2024).

¹⁶ Martin Dressel and George Grüner, *Electrodynamics of solids: optical properties of electrons in matter* (Cambridge University Press, 2002).

¹⁷ Dibyata Rout, Sanchayeta Ranajit Mudi, Marco Hoffmann, Sven Spachmann, Rüdiger Klingeler, and Surjeet Singh, “Structural and physical properties of trilayer nickelates $R_4Ni_3O_{10}$ (R = La, Pr, Nd),” *Phys. Rev. B* **102**, 195144 (2020).

¹⁸ Susmit Kumar, Øystein Fjellvåg, Anja Olafsen Sjåstad, and Helmer Fjellvåg, “Physical properties of Ruddlesden-Popper ($n = 3$) nickelate: $La_4Ni_3O_{10}$,” *Journal of Magnetism and Magnetic Materials* **496**, 165915 (2020).

¹⁹ Shangxiong Huangfu, Gawryluk Dariusz Jakub, Xiaofu Zhang, Olivier Blacque, Pascal Puphal, Ekaterina Pomjakushina, Fabian O. von Rohr, and Andreas Schilling, “Anisotropic character of the metal-to-metal transition in $Pr_4Ni_3O_{10}$,” *Phys. Rev. B* **101**, 104104 (2020).

²⁰ Nana Li, Jiayi Guan, Limin Yan, Xiaozhi Yan, Mingtao Li, Xuqiang Liu, Kai Zhang, Feiyu Li, Shu Cai, Haini Dong, Adama N-Diaye, Monica Amboage, Junjie Zhang, Yantao Cao, Hanjie Guo, Qingyu Kong, Liling Sun, and Wenge Yang, “Crystal and electronic structure studies of $La_4Ni_3O_{10-\delta}$ under high-pressure and low-temperature conditions,” *J. Am. Chem. Soc.* **147**, 43717–43726 (2025).

²¹ Atsushi Togo and Isao Tanaka, “First principles phonon calculations in materials science,” *Scripta Materialia* **108**, 1–5 (2015).

²² R. Boehler and J. Ramakrishnan, “Experimental results on the pressure dependence of the grüneisen parameter: a review,”

J. Geophys. Res. **85**, 6996–7002 (1980).

²³ R. J. Bruls, H. T. Hintzen, G. de With, R. Metselaar, and J. C. van Miltenburg, “The temperature dependence of the grüneisen parameters of MgSiN_2 , AlN and $\beta\text{-Si}_3\text{N}_4$,” *J. Phys. Chem. Solids* **62**, 783–792 (2001).

²⁴ M. Balkanski, R. F. Wallis, and E. Haro, “Anharmonic effects in light scattering due to optical phonons in silicon,” *Phys. Rev. B* **28**, 1928–1934 (1983).